PHYSICAL REVIEW C **98**, 014002 (2018)

Few-nucleon and many-nucleon systems with semilocal coordinate-space regularized chiral nucleon-nucleon forces

S. Binder,[1,2] A. Calci,[3] E. Epelbaum,[4] R. J. Furnstahl,[5] J. Golak,[6] K. Hebeler,[7] T. Hüther,[7] H. Kamada,[8] H. Krebs,[4] P. Maris,[9] Ulf-G. Meißner,[10,11,12] A. Nogga,[11] R. Roth,[7] R. Skibiński,[6] K. Topolnicki,[6] J. P. Vary,[9] K. Vobig,[7] and H. Witała[6]
(LENPIC Collaboration)
[1]*Department of Physics and Astronomy, University of Tennessee, Knoxville, Tennessee 37996, USA*
[2]*Physics Division, Oak Ridge National Laboratory, Oak Ridge, Tennessee 37831, USA*
[3]*TRIUMF, 4004 Wesbrook Mall, Vancouver, British Columbia, V6T 2A3, Canada*
[4]*Institut für Theoretische Physik II, Ruhr-Universität Bochum, D-44780 Bochum, Germany*
[5]*Department of Physics, The Ohio State University, Columbus, Ohio 43210, USA*
[6]*M. Smoluchowski Institute of Physics, Jagiellonian University, PL-30348 Kraków, Poland*
[7]*Institut für Kernphysik, Technische Universität Darmstadt, 64289 Darmstadt, Germany*
[8]*Department of Physics, Faculty of Engineering, Kyushu Institute of Technology, Kitakyushu 804-8550, Japan*
[9]*Department of Physics and Astronomy, Iowa State University, Ames, Iowa 50011, USA*
[10]*Helmholtz-Institut für Strahlen- und Kernphysik and Bethe Center for Theoretical Physics, Universität Bonn, D-53115 Bonn, Germany*
[11]*Institut für Kernphysik, Institute for Advanced Simulation and Jülich Center for Hadron Physics,*
Forschungszentrum Jülich, D-52425 Jülich, Germany
[12]*JARA-High Performance Computing, Forschungszentrum Jülich, D-52425 Jülich, Germany*

(Received 19 March 2018; revised manuscript received 21 June 2018; published 27 July 2018)

We employ a variety of *ab initio* methods, including Faddeev-Yakubovsky equations, no-core configuration interaction approach, coupled-cluster theory, and in-medium similarity renormalization group, to perform a comprehensive analysis of the nucleon-deuteron elastic and breakup reactions and selected properties of light and medium-mass nuclei up to ^{48}Ca using the recently constructed semilocal coordinate-space regularized chiral nucleon-nucleon potentials. We compare the results with those based on selected phenomenological and chiral EFT two-nucleon potentials, discuss the convergence pattern of the chiral expansion, and estimate the achievable theoretical accuracy at various chiral orders using an approach to quantify truncation errors of the chiral expansion without relying on cutoff variation. We also address the robustness of this method and explore alternative ways to estimate the theoretical uncertainty from the truncation of the chiral expansion.

DOI: 10.1103/PhysRevC.98.014002

I. INTRODUCTION

Nuclear forces have been extensively studied within the framework of chiral effective field theory (EFT) over the past two decades; see Refs. [1,2] for review articles. In this approach, two-, three-, and more-nucleon forces are calculated from the most general effective Lagrangian order by order in the chiral expansion, i.e., a perturbative expansion in powers of $Q \in \{p/\Lambda_b,\ M_\pi/\Lambda_b\}$ with p, M_π, and Λ_b referring to the magnitude of the typical nucleon three-momenta, the pion mass, and the breakdown scale, respectively.

Most of the calculations available so far utilize the heavy-baryon formulation of chiral EFT with pions and nucleons being the only active degrees of freedom and make use of Weinberg's power counting for contact interactions based on naive dimensional analysis [3,4]; see, however, Refs. [5–10] and references therein for alternative formulations. Much progress has been made within this framework in the past two years to improve the description of the nucleon-nucleon (NN) force. First, the order-Q^5 (i.e., N^{4}LO) [11] and even most of the order-Q^6 (N^{5}LO) contributions to the NN force have been worked out [12]. Second, a new generation of NN potentials up to N^{4}LO has been developed using semilocal [13,14] and nonlocal [15] regularization schemes; see also Refs. [16–19] for related studies along similar lines. In contrast to the previous order-Q^4 (N^{3}LO) chiral NN potentials of Refs. [20,21], the long-range part of the interaction introduced in Refs. [13,14] is regularized in coordinate space by multiplying with the function

$$f\left(\frac{r}{R}\right) = \left[1 - \exp\left(-\frac{r^2}{R^2}\right)\right]^n, \quad n = 6, \tag{1}$$

while the contact interactions are regularized in momentum space using a nonlocal Gaussian regulator with the cutoff $\Lambda = 2R^{-1}$. (See Refs. [16,18,22,23] for recently constructed chiral potentials with locally regularized long-range interactions.) The resulting semilocal coordinate-space regularized (SCS) chiral potentials are available for $R = 0.8$, 0.9, 1.0, 1.1, and 1.2 fm. The use of a local regulator for the short-range part of the interaction allows one to reduce the amount of finite-cutoff artifacts; see, however, Ref. [24] for a discussion of regulator artifacts in uniform matter. Furthermore, in contrast to the first generation of the chiral N^{3}LO potentials, all pion-nucleon

(πN) low-energy constants (LECs) were determined from the πN system without any fine tuning. Consequently, the long-range part of the NN force is predicted in a parameter-free way. In fact, clear evidence of the resulting (parameter-free) contributions to the two-pion exchange at orders Q^3 (i.e., N^{2}LO) and Q^5 was found in NN phase shifts [13,14]. We further emphasize that the approximate independence of the results for phase shifts on the functional form of the coordinate-space regulator in Eq. (1) was demonstrated in Ref. [13] at N^{3}LO by employing different exponents $n = 5$ and $n = 7$ and introducing an additional spectral function regularization with the momentum cutoff in the range of $\Lambda = 1$ to 2 GeV.

Very recently, a new family of semilocal momentum-space regularized (SMS) chiral NN potentials was introduced [25]. In addition to employing a momentum-space version of a local regulator for the long-range interactions and using the πN LECs from matching pion-nucleon Roy-Steiner equations to chiral perturbation theory [26] (see also Refs. [26–35] for related work on the determination of the πN LECs), the SMS potentials of Ref. [25] differ from the SCS ones of Ref. [13,14] in the determination of the NN contact interactions. That is, the SMS potentials of Ref. [25] were fitted directly to NN scattering data rather than to the Nijmegen partial wave analysis [36]. Another important difference concerns the implementation of the contact interactions. In particular, the SMS potentials of Ref. [25] utilize a specific choice for 3 redundant N^{3}LO contact operators out of 15, which parametrize the unitary ambiguity in the short-range part of the nuclear force at this chiral order. This is in contrast to the potentials of Refs. [13–15,20,21], where all 15 order-Q^4 contact interactions were fitted to Nijmegen PWA and/or NN scattering data.

Another important recent development is the establishment of a simple algorithm for estimating the theoretical uncertainty from the truncation of the chiral expansion [13]. The new method uses the available information on the chiral expansion of a given observable to estimate the magnitude of neglected higher order terms. To be specific, consider some few-nucleon observable $X(p)$ with p being the corresponding momentum scale. The chiral expansion of X up to order Q^n can be written in the form

$$X^{(n)} = X^{(0)} + \Delta X^{(2)} + \cdots + \Delta X^{(n)}, \tag{2}$$

where we have defined

$$\Delta X^{(2)} \equiv X^{(2)} - X^{(0)}, \quad \Delta X^{(i)} \equiv X^{(i)} - X^{(i-1)} \quad \text{for} \quad i \geqslant 3. \tag{3}$$

Assuming that the chiral expansion of the nuclear force translates into a similar expansion of the observable, one expects

$$\Delta X^{(i)} = \mathcal{O}(Q^i X^{(0)}). \tag{4}$$

In Ref. [13], the size of truncated contributions at a given order Q^i was then estimated via

$$\begin{aligned} \delta X^{(0)} &= Q^2 |X^{(0)}|, \\ \delta X^{(i)} &= \max_{2\leqslant j\leqslant i} (Q^{i+1}|X^{(0)}|,\ Q^{i+1-j}|\Delta X^{(j)}|) \ \text{ for } \ i \geqslant 2, \end{aligned} \tag{5}$$

subject to the additional constraint

$$\delta X^{(i)} \geqslant \max(|X^{(j\geqslant i)} - X^{(k\geqslant i)}|), \tag{6}$$

where the expansion parameter Q was chosen as

$$Q = \max\left(\frac{p}{\Lambda_b}, \frac{M_\pi}{\Lambda_b}\right). \tag{7}$$

For the breakdown scale of the chiral expansion Λ_b, the values of $\Lambda_b = 600$ MeV for $R = 0.8, 0.9$ and 1.0 fm, $\Lambda_b = 500$ MeV for $R = 1.1$ fm and $\Lambda_b = 400$ MeV for $R = 1.2$ fm were adopted based on an analysis of error plots [13]. Smaller values of the breakdown scale for softer cutoffs reflect an increasing amount of regulator artifacts.

The algorithm for uncertainty quantification specified above allows one to circumvent some of the drawbacks of the previous approach based on cutoff variation [21], such as the relatively narrow available range of cutoffs and the fact that residual regulator dependence shows the impact of neglected contact interactions, which contribute only at even orders Q^{2n} of the chiral expansion; see [13] for a comprehensive discussion. In addition, it provides an independent estimation of the theoretical uncertainty for any given cutoff value. This algorithm was already successfully applied in the two-nucleon sector. In particular, the actual size of the N^{4}LO corrections to NN phase shifts and scattering observables was shown in Ref. [14] to be in a good agreement with the estimated uncertainty at N^{3}LO [13]. A statistical interpretation of the theoretical error bars is discussed in Refs. [37,38]. For recent applications of this algorithm beyond the 2N system see Refs. [39–42].

The theoretical developments outlined above open the way for understanding and validating the details of the many-body forces and exchange currents that constitute an important frontier in nuclear physics. First steps along these lines were taken in Ref. [43] by employing the SCS NN potentials of Refs. [13,14] along with the algorithm for uncertainty quantification to analyze elastic nucleon-deuteron scattering and selected observables in ^{3}H, ^{4}He and ^{6}Li. To allow for a meaningful quantification of truncation errors in incomplete calculations based on NN interactions only, a slightly modified procedure for estimating the uncertainty at N^{2}LO and higher orders was adopted, by using for $i \geqslant 3$

$$\begin{aligned} \delta X^{(i)} = \max(&Q^{i+1}|X^{(0)}|,\ Q^{i-1}|\Delta X^{(2)}|, \\ &\times\ Q^{i-2}|\Delta X^{(3)}|,\ Q\delta X^{(i-1)}) \end{aligned} \tag{8}$$

instead of Eqs. (5) and (6); see Ref. [43] for more details. For many considered observables, the results at N^{2}LO and higher orders were then found to differ from experiment well outside the range of quantified uncertainties, thus providing a clear evidence for missing three-nucleon forces.[1] Furthermore, the magnitude of the deviations was found to be in agreement with the expected size of the chiral three-nucleon force (3NF) whose first contributions appear at N^{2}LO.

---

[1] We remind the reader that nuclear forces are scheme dependent and not directly measurable. Our conclusions regarding the expected size of three-body contributions refer to the framework we employ.

The same modified approach to error analysis was used recently in Ref. [44] to analyze the cross section and selected polarization observables for deuteron photodisintegration, nucleon-deuteron radiative capture and three-body ^{3}He photodisintegration and to study the muon capture rates in ^{2}H and ^{3}He. While these calculations are also incomplete as the 3NF was not included and the axial (electromagnetic) currents were only taken into account at the single-nucleon level (up to the two-nucleon level via the Siegert theorem), most of the considered observables were found to be in a good agreement with experimental data. For recent applications of the approaches to error analysis outlined above to nuclear matter properties and muonic deuterium see Refs. [45] and [46], respectively. These promising results provide important tests of the chiral potentials.

In this paper, we focus on the SCS chiral potentials of Refs. [13,14] and extend our earlier work [43] in various directions. First, in addition to elastic nucleon-deuteron scattering, we also study some of the most interesting breakup observables. We present the first applications of the SCS chiral NN potentials to light- and medium-mass nuclei beyond ^{6}Li using a variety of *ab initio* methods and discuss in detail the corresponding convergence pattern with respect to truncations of the model space. Last but not least, we address the limitations and robustness of the approach for uncertainty quantifications and consider some possible alternatives.

Our paper is organized as follows. Section II is devoted to the nucleon-deuteron elastic and breakup scattering reactions. Our results for light nuclei calculated by solving the Faddeev-Yakubovsky equations and/or using the No-Core Configuration Interaction (NCCI) method are presented in Sec. III, while those for medium-mass nuclei obtained within the coupled-cluster (CC) method and in-medium similarity renormalization group (IM-SRG) method are given in Sec. IV. Next, in Sec. V, we explore some alternative approaches for uncertainty quantification. Finally, the results of our work are summarized in Sec. VI.

II. NUCLEON-DEUTERON SCATTERING

A. Faddeev calculations

Neutron-deuteron (nd) scattering with neutrons and protons interacting via pairwise-interactions is described in terms of an amplitude $T|\phi\rangle$ satisfying the Faddeev-type integral equation [47,48]

$$T|\phi\rangle = tP|\phi\rangle + tPG_0T|\phi\rangle. \tag{9}$$

Here t represents the two-nucleon t-matrix, which is the solution of the Lippmann-Schwinger equation with a given NN interaction. The permutation operator $P = P_{12}P_{23} + P_{13}P_{23}$ is given in terms of the transposition operators, P_{ij}, which interchange nucleons i and j. The incoming state $|\phi\rangle = |\vec{q}_0\rangle|\phi_d\rangle$ describes the free nd motion with relative momentum $\vec{q}_0$ and the deuteron state $|\phi_d\rangle$. Finally, G_0 is the resolvent of the three-body center-of-mass kinetic energy. The amplitude for elastic scattering leading to the corresponding two-body final state $|\phi'\rangle$ is then given by [48,49]

$$\langle\phi'|U|\phi\rangle = \langle\phi'|PG_0^{-1}|\phi\rangle + \langle\phi'|PT|\phi\rangle, \tag{10}$$

while for the breakup reaction one has

$$\langle\phi_0'|U_0|\phi\rangle = \langle\phi_0'|(1+P)T|\phi\rangle, \tag{11}$$

where $|\phi_0'\rangle$ is the free three-body breakup channel state. We refer to Refs. [48–50] for a general overview of 3N scattering and for details on the practical implementation of the Faddeev equations.

When solving the 3N Faddeev Eq. (9), we include the NN force components with a total two-nucleon angular momenta $j \leqslant 5$ in 3N partial-wave states with the total 3N system angular momentum below $J \leqslant 25/2$. This is sufficient to get converged results for incoming neutron energies of $E_{\text{laboratory, n}} \leqslant 200$ MeV.

B. Elastic nd scattering

At low energies of the incoming neutron, the elastic nd scattering analyzing power A_y with polarized neutrons has been a quantity of great interest because predictions using standard high-precision NN potentials (AV18 [51], CDBonn

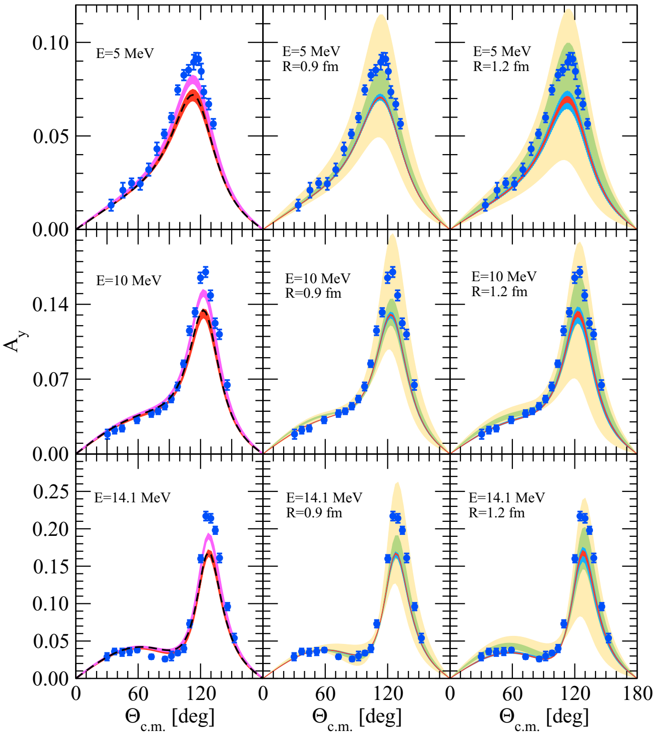

FIG. 1. The nd elastic scattering analyzing power A_y at $E_{\text{laboratory, n}} = 5$ MeV, 10 MeV, and 14.1 MeV. In the left panels the bottom (red) band covers predictions of standard NN potentials: AV18, CD Bonn, Nijm1 and Nijm2. The upper (magenta) band results when these potentials are combined with the TM99 3NF. The dashed (black) line shows prediction of the AV18+Urbana IX combination. In the middle (right) panel, predictions based on the SCS chiral NN potentials of Refs. [13,14] with the coordinate-space cutoff parameter $R = 0.9$ fm ($R = 1.2$ fm) are shown. The bands of increasing width show estimated theoretical uncertainty at N^{4}LO (red), N^{3}LO (blue), N^{2}LO (green), and NLO (yellow). The filled circles are nd data from Ref. [55] at 6.5 MeV, from Ref. [56] at 10 MeV, and from Ref. [57] at 14.1 MeV.

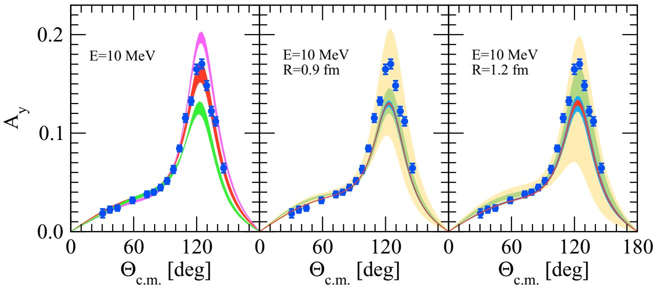

FIG. 2. The nd elastic scattering analyzing power A_y at $E_{\text{laboratory, n}} = 10$ MeV. In the left panel, bands of predictions for five versions of the old nonlocal chiral NN potentials of Refs. [21,58] at different orders of the chiral expansion are shown: NLO—the upper (magenta) band, N^{2}LO—the middle (red) band, and N^{3}LO—the bottom (green) band. These five versions correspond to different cutoff values used for the Lippmann-Schwinger equation and the spectral function regularizations, namely (450,500) MeV, (450,700) MeV, (550,600) MeV, (600,500) MeV, and (600,700) MeV. In the middle (right) panel, predictions based on SCS chiral NN potentials of Refs. [13,14] with the coordinate-space cutoff parameter of $R = 0.9$ fm ($R = 1.2$ fm) are shown. The bands of increasing width show estimated theoretical uncertainty at N^{4}LO (red), N^{3}LO (blue), N^{2}LO (green), and NLO (yellow). The full circles are nd data from Ref. [56] at 10 MeV.

[52], Nijm1 and Nijm2 [36]) fail to explain the experimental data for A_y. The data are underestimated by ∼30% in the region of the A_y maximum, which occurs at c.m. angles $\Theta_{\text{c.m.}} \sim 125^\circ$. Combining standard NN potentials with commonly used models of a 3NF, such as the Tucson-Melbourne (TM99) [53] or Urbana IX [54] models, removes approximately only half of the discrepancy (see left column in Fig. 1).

Using the old, nonlocally regularized chiral NN potentials of Refs. [21,58], the predictions for A_y vary with the order of the chiral expansion. In particular, as reported in Ref. [59], the NLO results overestimate the A_y data while the N^{2}LO NN forces seem to be in quite a good agreement with experiment; see Fig. 2. Only when the N^{3}LO NN chiral forces are used does a clear discrepancy between theory and data emerge in the region of A_y maximum, which is similar to the one for standard forces. This is visualized for $E_n = 10$ MeV in the left panel of Fig. 2, where bands of predictions correspond to five versions of the nonlocal NLO, N^{2}LO and N^{3}LO potentials of Refs. [21,58], which differ from each other by the cutoff parameters used for the Lippmann-Schwinger equation and the spectral function regularizations. Such a behavior of A_y predictions at different orders in the chiral expansion can be traced back to a high sensitivity of A_y to ^3P_j NN force components [60,61], which are accurately reproduced for the old nonlocal chiral potentials of Refs. [21,58] only at N^{3}LO. This is visualized in the left panel of Fig. 3. Contrary to the observed behavior of old potentials of Refs. [21,58], the predictions for A_y based on the SCS NN chiral forces turn out to be similar to those of the high-precision phenomenological potentials already starting from NLO; see the middle and right panels of Figs. 1 and 2. This reflects the considerably improved convergence with the order of the chiral expansion of the semilocal potentials, as visualized in the middle and right panels of Fig. 3 for the case of the $^3P_2$ phase shift. Only LO values are far away from the empirical values while the NLO results already turn out to be very close to those of the Nijmegen partial wave analysis (NPWA) at energies below ≈40 MeV. The N^{2}LO, N^{3}LO, and N^{4}LO results for the phase shifts overlap with each other and with the NPWA values. The corresponding A_y predictions at orders above LO are very close to each other as seen in the middle and right panels of Figs. 1 and 2. Notice that the results for the two different cutoff values are very similar, the feature which holds true also for other considered scattering observables. The somewhat wider error bands for the softest choice of the regulator reflect the estimated lower breakdown scale of $\Lambda_b = 400$ MeV.

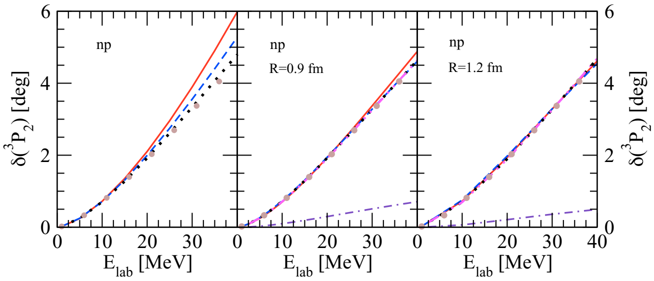

FIG. 3. The neutron-proton ^3P_j phase-shifts as a function of laboratory energy E_{lab}. In the left panel the solid (red), dashed (blue), and dotted (black) lines show predictions of the old chiral Bochum NLO, N^{2}LO, and N^{3}LO NN potentials of Refs. [21,58] with the cutoff parameters of (600,500) MeV. In the middle (right) panel the indigo dashed-dotted, red solid, blue dashed, black dotted and magenta dashed-double-dotted lines are predictions of SCS chiral potentials with local regulator and parameter $R = 0.9$ fm ($R = 1.2$ fm) at LO, NLO, N^{2}LO, N^{3}LO, and N^{4}LO, respectively. The brown solid circles are experimental Nijmegen phase-shifts [60,61].

It is instructive to look at the estimated theoretical uncertainty from the truncation of the chiral expansion shown in the right panels of Figs. 1 and 2. Notice that our calculations for three- and more-nucleon observables are incomplete starting from N^{2}LO due to the missing 3NFs. The width of the bands calculated using Eqs. (5) and (6) at LO and NLO and using Eq. (8) starting from N^{2}LO show our estimations of the expected theoretical uncertainties *after* inclusion of the corresponding 3NF contributions. At the considered low energies, the theoretical uncertainty decreases quite rapidly so that one expects precise predictions for A_y starting from N^{3}LO.[2] Interestingly, our approach to uncertainty quantification is capable of accounting for the already mentioned strongly fine-tuned nature of this observable which results in a large theoretical uncertainty at NLO. Notice that the experimental data are

---

[2] We emphasize, however, that the usage of Eq. (8) in the incomplete calculations presented here may lead to underestimation of the theoretical uncertainty at higher orders. A more reliable estimation of the truncation error is expected from performing complete calculations that include 3NFs and using Eqs. (5) and (6) at all orders. This work is in progress.

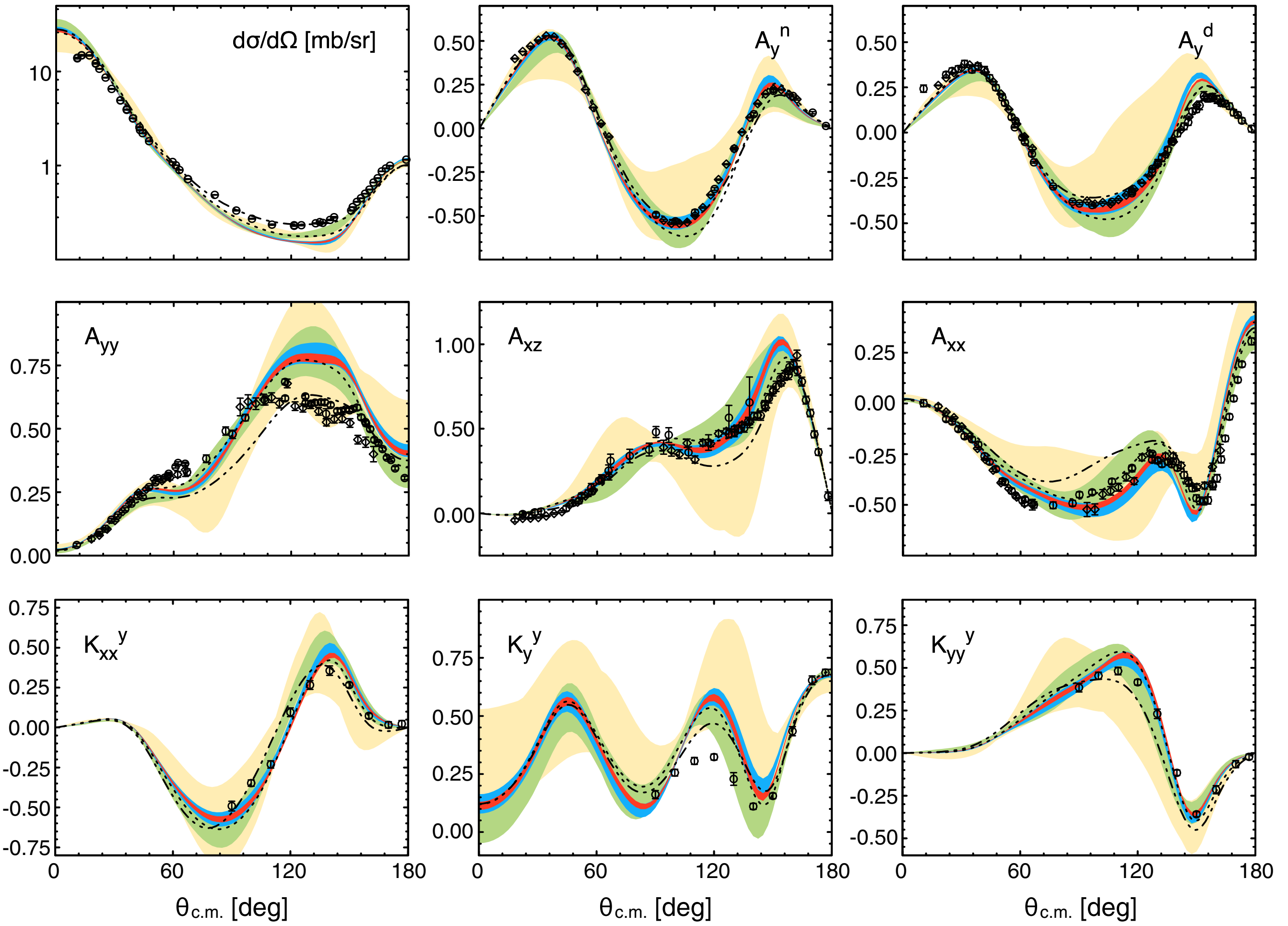

FIG. 4. Predictions for the differential cross section, nucleon and deuteron vector analyzing powers A_y^n and A_y^d, deuteron tensor analyzing powers A_{yy}, A_{xz}, and A_{xx} and polarization-transfer coefficients $K_{xx}^{y'}$, $K_y^{y'}$, and $K_{yy}^{y'}$ at the laboratory energy of 135 MeV based on the NN potentials of Refs. [13,14] for $R = 0.9$ fm without including the 3NF. The bands of increasing width show estimated theoretical uncertainty at N^{4}LO (red), N^{3}LO (blue), N^{2}LO (green), and NLO (yellow). The dotted (dashed) lines show the results based on the CD Bonn NN potential (CD Bonn NN potential in combination with the Tucson-Melbourne 3NF). Open circles (diamonds) are proton-deuteron data from Refs. [63–66] (Refs. [138]).

correctly described at this order within the errors. It remains to be seen upon the inclusion of the 3NF and performing complete calculations whether the A_y-puzzle will survive at higher orders of the chiral expansion. Notice further that at N^{4}LO, the 3NF involves purely short-range contributions with two derivatives, which affect nucleon-deuteron (Nd) P-waves [62]. It is conceivable that the inclusion of such terms will lead to a proper description of A_y once the corresponding LECs are tuned to reproduce Nd scattering observables.

Apart from A_y and the deuteron tensor analyzing power iT_{11}, which is known to show a similar behavior to A_y, there is not much room for three-nucleon force effects in elastic Nd scattering at low energies; see Ref. [43] for the predictions of other observables at 10 MeV. However, significant disagreements with the data start to appear at intermediate energies of ~50 MeV and higher. As a representative example, we show in Fig. 4 our predictions for selected elastic scattering observables at 135 MeV. In addition to the well-known underestimation of the differential cross section minima, the spin-observables calculated using the NN interactions only start to show deviations from the data. These deviations tend to increase with energy; see [67] for a comprehensive discussion. As shown in Ref. [43], the theoretical uncertainty of the chiral EFT results at N^{3}LO and N^{4}LO is considerably smaller than the observed disagreements between the predictions based on the NN forces and the experimental data even at energies of the order of 200 MeV. Our results suggest that elastic Nd scattering in the energy range of ~50–200 MeV is very well suited to study the detailed structure of the chiral 3NF.

C. Nd breakup

Among numerous kinematically complete configurations of the Nd breakup reaction the so-called symmetric space star (SST) and quasifree scattering (QFS) configurations have attracted special attention. The cross sections for these geometries are very stable with respect to the underlying dynamics. To be specific, different phenomenological potentials,

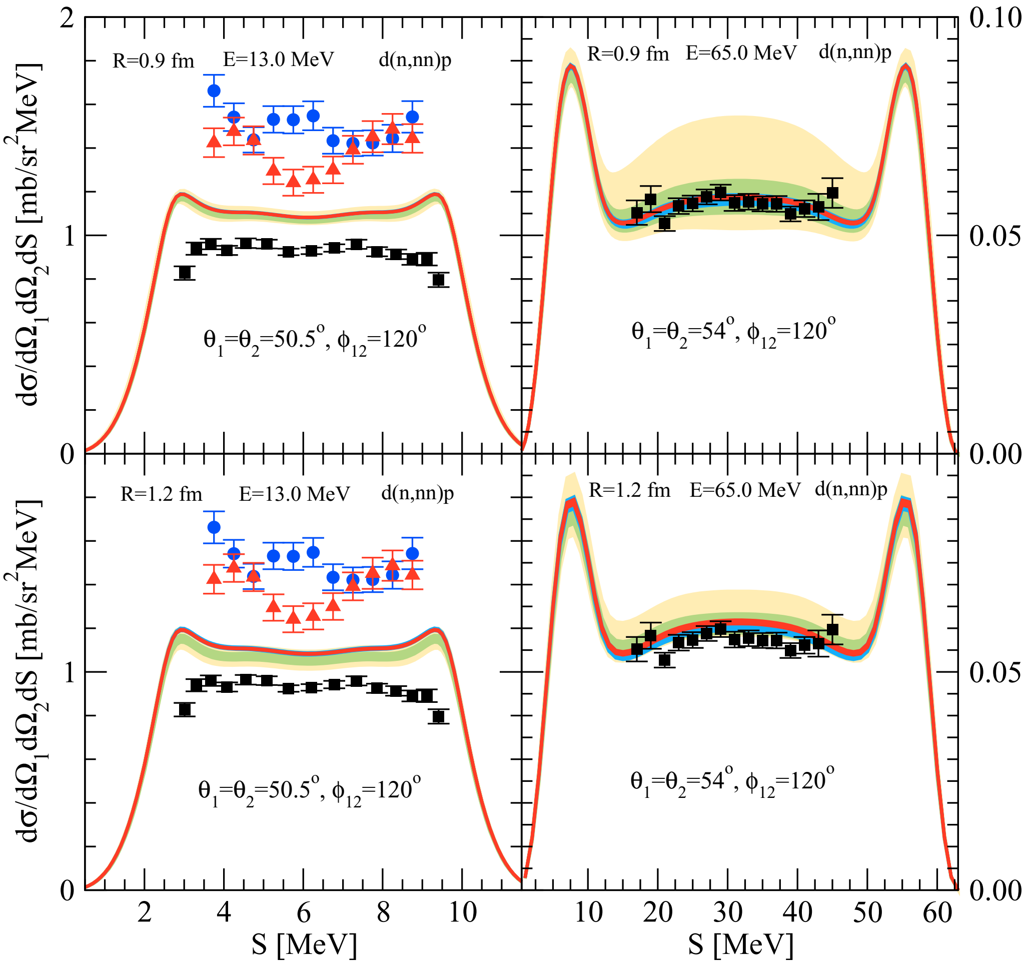

FIG. 5. The SST nd breakup cross sections at incoming neutron laboratory energy $E_{\text{laboratory, n}} = 13$ MeV (left graphs) and 65 MeV (right graphs), as a function of the arc-length S along the kinematical locus in the E_1-E_2 plane. Upper and lower graphs show the results based on the SCS chiral NN potentials of Refs. [13,14] with the cutoff $R = 0.9$ fm and $R = 1.2$ fm, respectively The bands of increasing width show estimated theoretical uncertainty at N^{4}LO (red), N^{3}LO (blue), N^{2}LO (green), and NLO (yellow). (Blue) circles and (red) triangles are nd data from Refs. [73] and [74,75], respectively. Proton-deuteron experimental data are shown as (black) squares. At 13 MeV (65 MeV) the pd data are from Ref. [76] (Ref. [77]).

alone or combined with standard 3NFs, lead to very similar results for the cross sections [68] which deviate significantly from the available SST and neutron-neutron (nn) QFS data. At low energies, the cross sections in the SST and QFS configurations are dominated by the S-waves. For the SST configuration, the largest contribution to the cross section comes from the $^3S_1$ partial wave, while for the nn QFS the $^1S_0$ partial wave dominates. Neglecting rescattering, the QFS configuration resembles free NN scattering. For elastic low-energy neutron-proton (np) scattering one expects contributions from the $^1S_0$ np and $^3S_1$ force components. For elastic nn scattering, only the $^1S_0$ nn channel is allowed by the Pauli principle. This suggests that the nn QFS is a powerful tool to study the nn interaction. The measurements of np QFS cross sections have revealed a good agreement between the data and theory [69], thus confirming the knowledge of the np force. However, for the nn QFS, it was found that the theory underestimates the data by ∼20% [69,70]. The stability of the QFS cross sections with respect to the underlying dynamics means that, assuming correctness of the nn QFS data, the present day $^1S_0$ nn interaction is probably incorrect [68,71,72].

In Fig. 5, we compare predictions of the SCS chiral potentials at different orders to the SST cross section data at two incoming nucleon energies $E = 13$ MeV and 65 MeV for the cutoffs $R = 0.9$ fm and $R = 1.2$ fm. At 65 MeV the theoretical uncertainty is large at NLO but decreases rapidly at higher orders of the chiral expansion. One expects accurate predictions at N^{3}LO and N^{4}LO. Given the good agreement with the experimental data of Ref. [77] as visualized in the right panel of Fig. 5, there is not much room for 3NF effects for this observable. At 13 MeV, the uncertainty bands are rather narrow at all considered orders, which is especially true for the cutoff choice of $R = 0.9$ fm, but the nd and proton-deuteron (pd) breakup data are far away from the theory. The two nd data sets are from different measurements and both show a significant disagreement with our theoretical results, even though the data seem to be inconsistent with each other for the values of the kinematical locus variable S in the range of $S = 5 \ldots 7$ MeV.

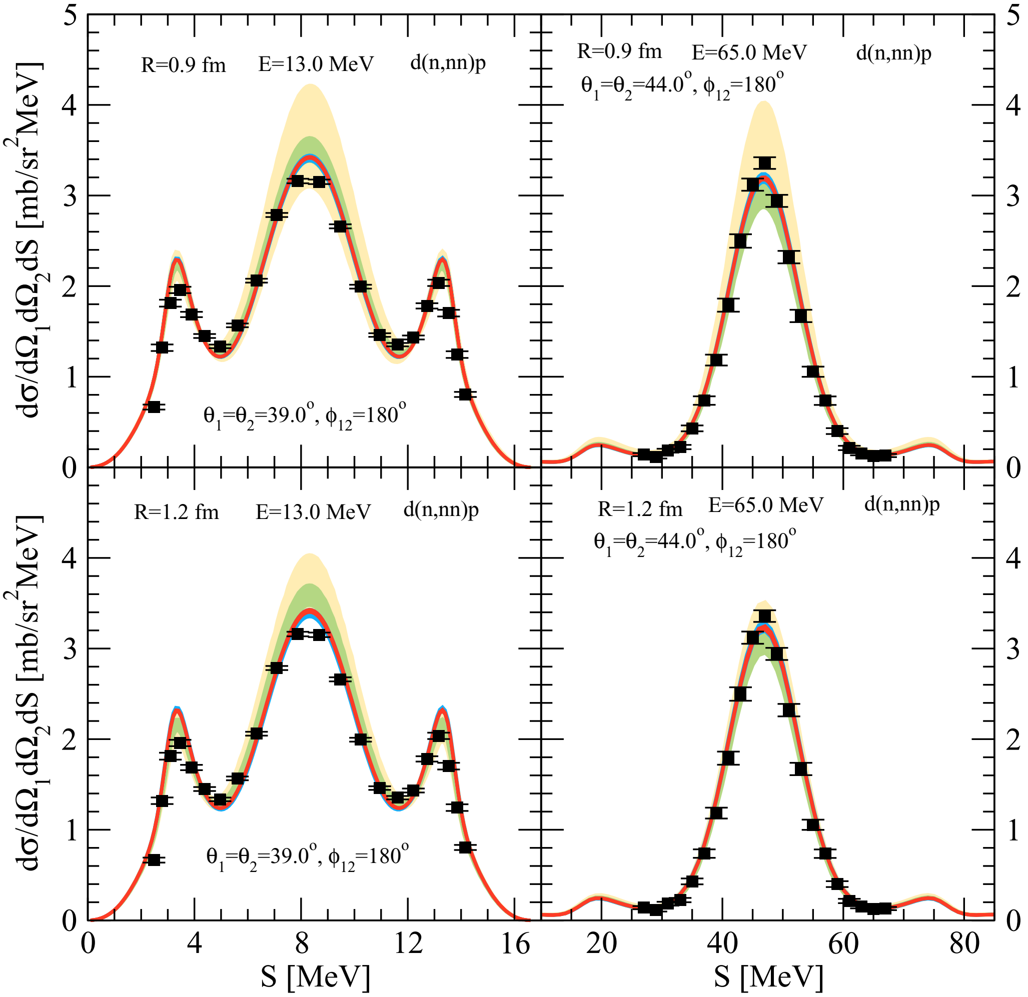

FIG. 6. Same as described in the caption of Fig. 5 but for the QFS nd breakup configuration. The pd data at 65 MeV are from Ref. [78]. For remaining notation see Fig. 5.

The pd data set shown in the left panel of Fig. 5 is supported by other SST pd breakup measurements [79] in a similar energy range. The calculations of the pd breakup with inclusion of the pp Coulomb force [80] revealed only very small Coulomb force effects for this configuration. Since, at that energy, the SST configuration is practically dominated by the S-wave NN force components, the big difference between pd and nd data seems to indicate a large charge-symmetry breaking in the $^1S_0$ NN partial wave. We anticipate it to be very difficult to explain the large difference between the nd and pd data sets by the inclusion of a 3NF without introducing large charge symmetry breaking interactions. Furthermore, the discrepancy between the theory and experimental pd data is puzzling. It remains to be seen whether the inclusion of the chiral 3NF will affect the results for the pd SST configuration at this energy.

For the nn QFS geometry, we show in Figs. 6 and 7 the predictions based on the SCS chiral potentials at $E = 13$ MeV, 65 MeV, and 156 MeV, together with the available pd breakup data. In the latter case, we refrain from showing the results corresponding to the softest cutoff of $R = 1.2$ fm given the rather high energy. Again the theoretical uncertainty rapidly decreases with an increasing order of the chiral expansion, leading to very precise predictions at N^{3}LO and N^{4}LO, which, in addition, agree well with the pd breakup data. Assuming that the agreement will hold after the inclusion of the corresponding 3NF, this provides, together with the drastic ≈20% underestimation of nn QFS data found in Refs. [69,70], yet another indication of our poor knowledge of low energy $^1S_0$ neutron-neutron force.

Finally, in Figs. 8 and 9, the results for the nucleon analyzing power A_y in the SST and nn QFS geometries of the Nd breakup reaction at 13 MeV and 65 MeV are presented. Again, the band widths of theoretical uncertainties become quite narrow with an increasing order of chiral expansion. There appears to be reasonable agreement between experiment and theory without 3NF contributions given the large error bars of the available data.

III. LIGHT NUCLEI

A. Faddeev–Yakubovsky calculations

For the $A = 3$ and $A = 4$ bound state calculations, we solve Faddeev and Yakubovsky equations, respectively. These

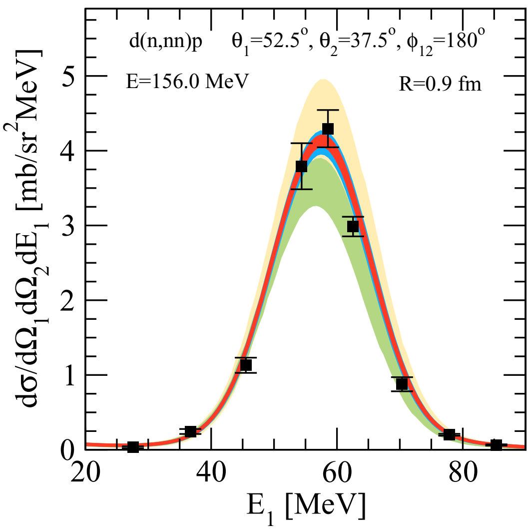

FIG. 7. The nn QFS pd breakup cross section at incoming neutron laboratory energy $E_{\text{laboratory, n}} = 156$ MeV as a function of the energy E_1 in the E_1-E_2 plane. The bands of increasing width show estimated theoretical uncertainty at N^{4}LO (red), N^{3}LO (blue), N^{2}LO (green) and NLO (yellow) based on the SCS chiral NN potentials of Refs. [13,14] with local regulator and parameter $R = 0.9$ fm. The (black) squares are pd data of Ref. [81].

calculations are performed in momentum space, which enables us to obtain high accuracies for binding energies and also for the properties of the wave function.

For $A = 3$, similar to the 3N scattering case, we rewrite the Schrödinger equation into Faddeev equations

$$|\psi\rangle = G_0\, t\, P\, |\psi\rangle. \tag{12}$$

Here, $|\psi\rangle$ denotes the Faddeev component. The 3N wave function is related to the Faddeev component by $|\Psi\rangle = (1 + P)\,|\psi\rangle$. In contrast to the 3N scattering problem, no singularities show up for bound states since the energy is negative and below the binding energy of the deuteron.

We represent the equation using partial wave decomposed momentum eigenstates

$$|p_{12}\, p_3\, \alpha\rangle = \big|p_{12}\, p_3 \left[(l_{12}s_{12})j_{12}\big(l_3\tfrac{1}{2}\big)I_3\right]J_3\ \big(t_{12}\tfrac{1}{2}\big)T_3\big\rangle, \tag{13}$$

where p_{12}, l_{12}, s_{12}, t_{12}, and j_{12} are the magnitude of the momentum, the orbital angular momentum, the spin, the isospin and the total angular momentum of the subsystem of nucleons 1 and 2. p_3, l_3, and I_3 denote the magnitude of the momentum, the orbital angular momentum and the total angular momentum of the spectator nucleon relative to the (12) subsystem, respectively. The angular momenta and isospin quantum numbers are coupled together with the spin and isospin $\frac{1}{2}$ of the third nucleon to the total angular momentum $J_3 = \frac{1}{2}$ and isospin T_3. For the results shown below, we take angular momenta up through $j_{12} = 7$ and $T_3 = \frac{1}{2}$ and $\frac{3}{2}$ states into account. We adopt $N_{12} = N_3 = 64$ mesh points for the discretization of the momenta between 0 and $p_{\max} = 15\ \text{fm}^{-1}$. We note that the solution of the Lippmann-Schwinger equation for t requires a more extended momentum grid up to momenta of 35 fm^{-1}. We find that this choice of momenta guarantees that our numerical accuracy is better than 1 keV for the binding energy and, for the 3N systems, also the expectation values of the Hamiltonian H. The latter ones require the calculation of wave functions and are therefore more difficult to obtain. We take isospin breaking of the nuclear interaction into account. For the SCS chiral interactions, we add the point Coulomb interaction in pp. The contribution of the neutron/proton mass difference is later treated perturbatively and given in Table II. For the calculation of the binding energies and wave functions, we use an averaged mass of $m_N = 938.918$ MeV. More details on the computational aspects can be found in Ref. [82]. Results for the binding energies are summarized in Table I.

To provide benchmark results, we also summarize expectation values for the kinetic energy, the potential, the point proton and neutron rms radii and probabilities for S-, P-, and D-states in Table II. Here, we restrict ourselves to N^{4}LO and ^{3}H and compare to results of two phenomenological interactions, AV18 and CDBonn, and to ones based on the older series of chiral interactions of Ref. [21] [$\Lambda, \tilde{\Lambda} = (600,\ 700)$ MeV] and the chiral interaction of Ref. [20]. Note that we have used, for the calculations with these forces, the EM interaction of AV18 [51] acting in pp and nn to be consistent with previous calculations. The deviation of the binding energy E and expectation value $\langle H\rangle$ of the Hamiltonian is due to the contribution of the mass difference of the proton and neutron to the kinetic energy $\langle T_{\text{CSB}}\rangle$, which we take into account for the calculation of $\langle H\rangle$ but which we do not consider for the solution of the Faddeev equations. We checked that results for ^{3}He are close to the results for ^{3}H except that the sign of the contribution of the proton/neutron mass difference is opposite and proton and neutron radii are interchanged, as expected for mirror nuclei. Because the convergence with respect to partial waves of the Faddeev component is faster, it is advantageous to project on Faddeev components whenever possible. Therefore, the wave function and Faddeev component are normalized to $3\langle\Psi|\psi\rangle = 1$. The results for the norm $\langle\Psi|\Psi\rangle$ show that our representation of the wave function includes 99.9% of the wave function. Nevertheless, we evaluate the kinetic energy using again the faster convergence for overlaps of Faddeev component and wave function by $\langle T\rangle = 3\langle\Psi|\, T\, |\psi\rangle$. A similar trick for the potential operator is not possible and not necessary since the potential operator suppresses contributions of high angular momenta due to its finite range. Note that our choice of normalization ensures that the relevant partial waves are properly normalized and, therefore, the calculation of the expectation values does not require a division by the norm of the wave function.

Comparing the new results to those from nonlocal chiral interactions of Ref. [21], the kinetic energies tend to be larger now. But they only become comparable to a standard local phenomenological interaction like AV18 for smaller configuration-space regulators R. For larger R, the expectation values are in better agreement with nonlocal interactions like CDBonn. Generally, the observed pattern indicates that the new interactions induce more NN short-range correlations than the chiral interactions of Refs. [20,21] but, at least for larger R, still less than phenomenological ones. Notice that the kinetic energies at N^{3}LO, which are not shown explicitly, are found to take similar values, while those at NLO and N^{2}LO appear to be

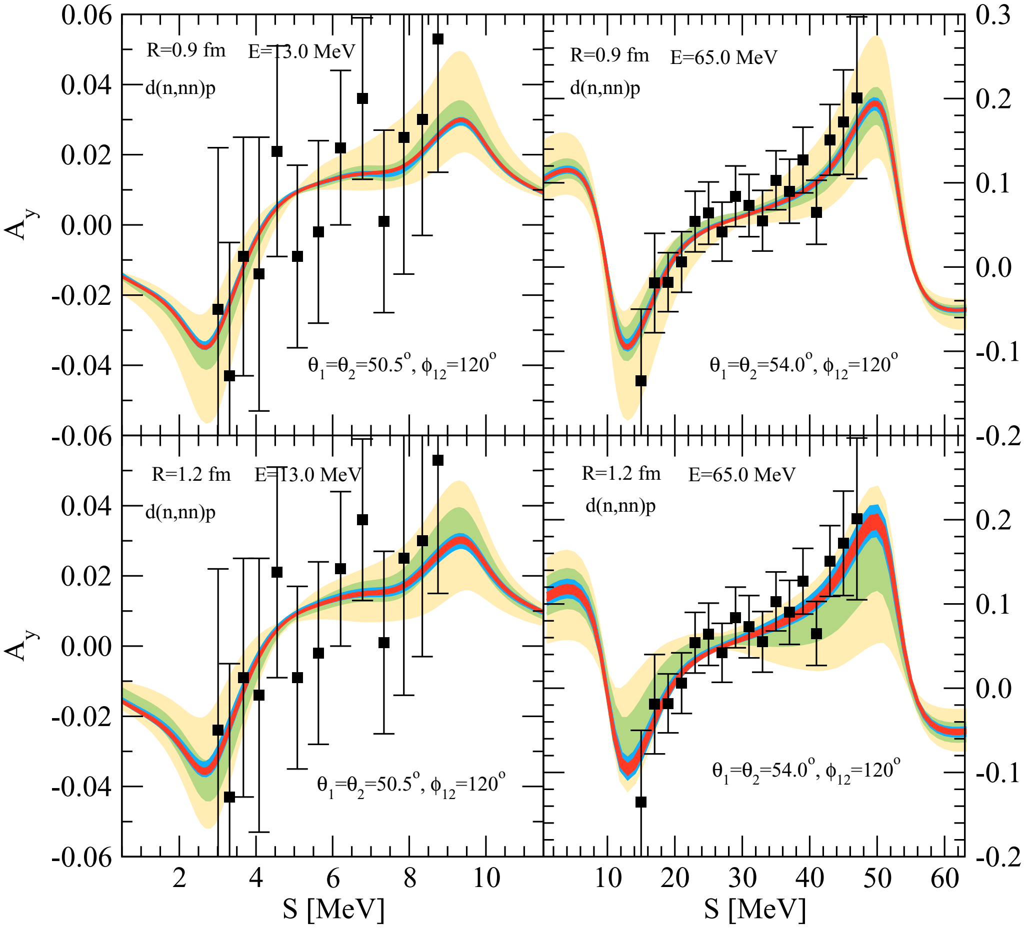

FIG. 8. The SST pd analyzing power at incoming neutron laboratory energy $E_{\text{laboratory, n}} = 13$ MeV (left panel) and 65 MeV (right panel), as a function of the arc-length S along the kinematical locus in the E_1-E_2 plane. The bands of increasing width show estimated theoretical uncertainty at N^{4}LO (red), N^{3}LO (blue), N^{2}LO (green) and NLO (yellow) based on the SCS chiral NN potentials of Refs. [13,14] with local regulator and the cutoff parameters of $R = 0.9$ fm (upper graphs) and $R = 1.2$ fm (lower graphs). In the left panel the (black) squares are pd data of Ref. [76]. In the right panel the (black) squares are pd data of Ref. [77].

significantly smaller. These findings are in line with the nonperturbative nature of the SCS potentials at N^{3}LO and N^{4}LO as found in the Weinberg eigenvalue analysis of Ref. [83]. As demonstrated in Ref. [25], this feature can be traced back to the large values of the LECs accompanying the redundant N^{3}LO contact interactions in the $^1S_0$ and $^3S_1$-$^3D_1$ channels.

The contributions of the *D*-wave component of the wave function is of the order of 6-7%, which is comparable to the nonlocal and older chiral interactions but smaller than results for AV18. We note that the *D*-state probability increases with increasing *R*. This is a feature of the higher-order interactions at N^{3}LO and N^{4}LO. The lower order interactions show the opposite behavior. We found that the proton and neutron rms radii are not strongly affected by the regulator *R*. This is in line with the observation that the binding energies at this order are quite independent of the cutoff. Nevertheless, it is interesting that the radii do not appear to be strictly correlated to the binding energies. We expected that in this situation, where subtle effects affect the radii, the changes are driven by the repulsiveness of the interaction at short distances and therefore correlated with the kinetic energy. But even this is not supported by the results. At lower orders from LO to N^{2}LO, the binding energies depend much stronger on the cutoff, and one finds the usual correlation of binding energy and radius.

For $A = 4$, we can rewrite the Schrödinger equation into Yakubovsky equations for the two Yakubovsky components $|\psi_1\rangle$ and $|\psi_2\rangle$. Again, we can recover the wave function by applications of permutation operators $|\Psi\rangle = [1 - (1 + P)P_{34}](1 + P)|\,\psi_1\,\rangle + (1 + P)(1 + \tilde{P})|\psi_2\rangle$. In addition to the sum of cyclic and anticyclic permutations used in the 3N system, we also need a transposition of nucleons 3 and 4, P_{34}, and the interchange of the subsystems (12) and (34) given by $\tilde{P} = P_{13}P_{24}$. The two coupled Yakubovsky equations then read

$$|\psi_1\rangle = G_0\, t\, P\, [(1 - P_{34})|\psi_1\rangle + |\psi_2\rangle], \tag{14}$$

$$|\psi_2\rangle = G_0\, t\, \tilde{P}\, [(1 - P_{34})|\psi_1\rangle + |\psi_2\rangle]. \tag{15}$$

Here, G_0 and t are, again, the free propagator and NN t-matrix respectively. It is understood that they are embedded into the 4N Hilbert space for this application.

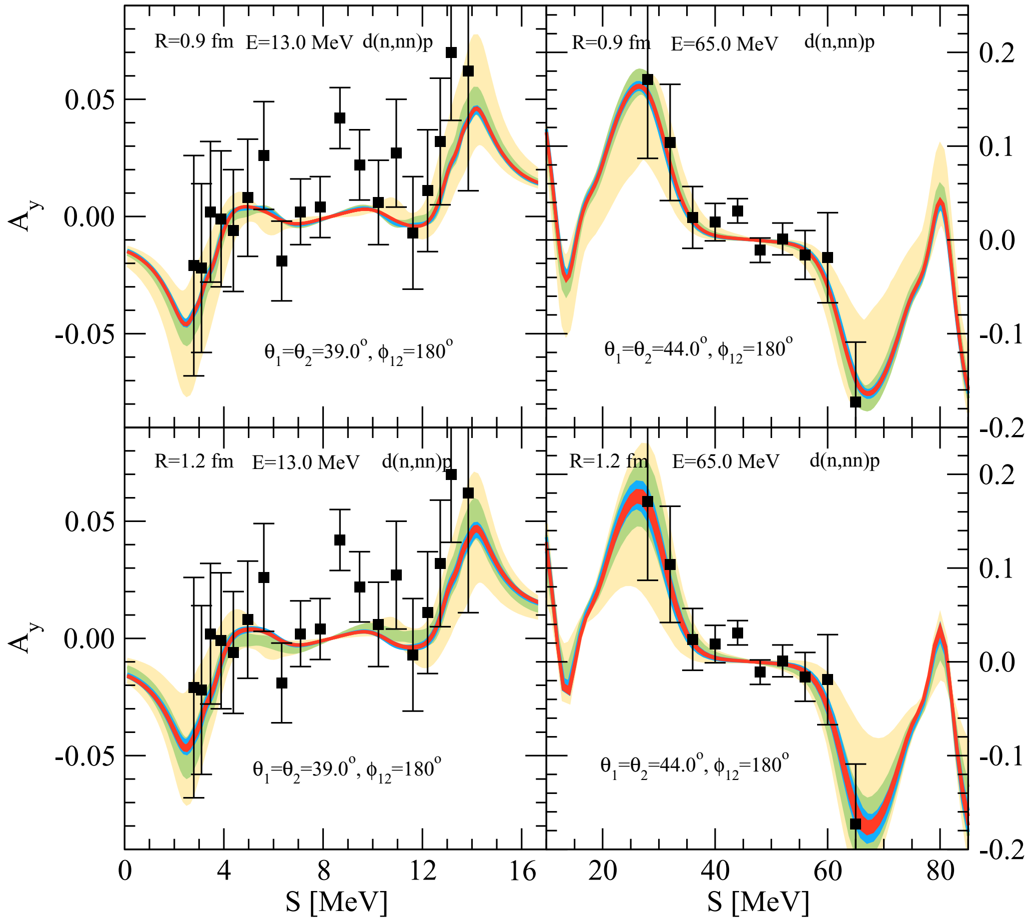

FIG. 9. Same as described in the caption of Fig. 8 for the QFS nd breakup configurations of Fig. 6.

We again solve the equations in momentum space using a partial-wave decomposed basis. The form of the equations guarantees a rather fast convergence with respect to partial waves if the two Yakubovsky components are expressed in different basis sets. The first component is expanded in a set of Jacobi momenta that separate the (12) subsystem (p_{12}), the motion of the third nucleon relative to (12) (p_3) and the fourth nucleon relative to the (123) subsystem (q_4),

$$|p_{12}\,p_3\,q_4\,\alpha\rangle = \big|p_{12}\,p_3\,q_4\,\big\{\big[(l_{12}s_{12})j_{12}\big(l_3\tfrac{1}{2}\big)I_3\big] \times J_3\big(l_4\tfrac{1}{2}\big)\,I_4\,\big\}J_4\,\big[\big(t_{12}\tfrac{1}{2}\big)T_3\tfrac{1}{2}\big]T_4\big\rangle. \quad (16)$$

In addition to the quantities defined for the 3N system, we require the orbital angular momentum corresponding to the momentum of the fourth particle l_4, its total angular momentum I_4 and the total angular momentum and isospin of the 4N system, J_4 and T_4, respectively. We refer to this set of basis states as 3+1 coordinates. $|\psi_2\rangle$ is expanded in states introducing relative momenta within the subsystems (12) and (34), p_{12} and p_{34}, respectively, and the relative momentum of these two subsystems q,

$$|p_{12}\,p_{34}\,q\,\alpha\rangle = \big|p_{12}\,p_{34}\,q\,\{[(l_{12}s_{12})j_{12}\lambda]\,I\,(l_{34}s_{34})j_{34}\} \times J_4\,\big[(t_{12}t_{34})\tfrac{1}{2}\big]T_4\big\rangle. \quad (17)$$

The angular momenta, spin, and isospin of the (34) system are given by l_{34}, s_{34}, j_{34}, and t_{34}. The angular dependence of the q momentum is expanded in orbital angular momenta λ. The angular momenta are coupled as indicated by brackets to the total 4N angular momentum $J_4 = 0$ and isospin $T_4 = 0$. Below, we refer to these basis states as 2+2 coordinates.

TABLE I. Calculated ^{3}H and ^{3}He binding energies using chiral NN interactions at different orders of the chiral expansion and at five different values of R. Energies are given in MeV.

R [fm]	LO	NLO	N^{2}LO	N^{3}LO	N^{4}LO
^{3}H					
0.8	−12.038	−8.044	−8.039	−7.569	−7.489
0.9	−11.747	−8.216	−8.146	−7.575	−7.600
1.0	−11.295	−8.380	−8.282	−7.534	−7.642
1.1	−10.822	−8.554	−8.428	−7.514	−7.630
1.2	−10.394	−8.727	−8.579	−7.481	−7.580
^{3}He					
0.8	−11.151	−7.312	−7.303	−6.867	−6.794
0.9	−10.862	−7.472	−7.402	−6.875	−6.897
1.0	−10.423	−7.624	−7.528	−6.837	−6.935
1.1	−9.968	−7.786	−7.664	−6.816	−6.923
1.2	−9.561	−7.948	−7.806	−6.783	−6.876

TABLE II. Binding energy E, expectation values of the Hamiltonian $\langle H\rangle$, the kinetic energy $\langle T\rangle$, the potential energy $\langle V\rangle$, and the contribution of the mass difference of proton and neutron to the kinetic energy $\langle T_{\mathrm{CSB}}\rangle$ for ^{3}H at order N^{4}LO. The calculated norm of the wave function and probabilities for S-, P-, and D-states are also shown. Finally, we also list results for the point proton and neutron rms radii r_p and r_n. Energies are given in MeV (except for the $\langle T_{\mathrm{CSB}}\rangle$ which is given in keV), radii in fm and probabilities in %.

R [fm]	E	$\langle H\rangle$	$\langle T\rangle$	$\langle V\rangle$	$\langle T_{\mathrm{CSB}}\rangle$	$\langle\Psi\vert\Psi\rangle$	$P(S)$	$P(P)$	$P(D)$	r_p	r_n
0.8	−7.489	−7.499	53.59	−61.08	−9.48	0.9989	93.95	0.033	6.02	1.675	1.849
0.9	−7.600	−7.608	48.45	−56.05	−8.45	0.9993	93.91	0.034	6.06	1.669	1.838
1.0	−7.642	−7.649	44.30	−51.94	−7.70	0.9995	93.70	0.035	6.27	1.670	1.838
1.1	−7.630	−7.637	40.74	−48.37	−7.08	0.9996	93.16	0.040	6.80	1.678	1.845
1.2	−7.580	−7.587	37.57	−45.15	−6.52	0.9998	92.58	0.046	7.37	1.689	1.858
AV18	−7.620	−7.626	46.71	−54.34	−6.75	0.9988	91.43	0.066	8.51	1.653	1.824
CDBonn	−7.981	−7.987	37.59	−45.57	−5.85	0.9996	92.93	0.047	7.02	1.614	1.775
N^{2}LO [21]	−7.867	−7.872	31.85	−39.72	−5.11	0.9995	93.43	0.039	6.53	1.624	1.787
Idaho N^{3}LO [20]	−7.840	−7.845	34.52	−42.36	−5.52	0.9998	93.65	0.037	6.32	1.653	1.812

We again use 64 mesh points for the discretization of the momenta up to 15 fm^{-1}. The only exception is the q momentum where 48 mesh points were sufficient to get binding energies with a accuracy better than 10 keV and the expectation value of the Hamiltonian with an accuracy of better than 50 keV. Again the two-body angular momentum is restricted to $j_{12}^{\max} = 7$. We also restrict all orbital angular momenta to 8 and the sum of all angular momenta to 16. For the four-body calculations, we assume that the ^{4}He system is a pure $T_4 = 0$ state. The neutron/proton mass difference does not contribute in this case. More details on the computational aspects can again be found in [82]. Results for the binding energies of the ground state are summarized in Table III. Notice that we predict a bound excited state for the leading order interactions. The binding energies for these excited states vary between −12.6 and −10.4 MeV depending on the regulator parameter R. This second bound state disappears at higher orders.

For N^{4}LO, we also show expectation values of the Hamiltonian, the kinetic energy, the potential and the point proton rms radius in Table IV. We again compare our results to AV18, CD-Bonn and the two older chiral interactions. The Yakubovsky components, as the Faddeev component for the 3N system, converge much faster with respect to partial waves than the wave function. Therefore, we normalize the wave function using the relation $12\langle\psi_1|\Psi\rangle + 6\langle\psi_2|\Psi\rangle = 1$ and calculate the kinetic energy using a corresponding overlap of the wave function and the Yakubovsky components in the coordinates natural for the Yakubovsky component involved. The wave function itself can be expanded in 3+1 or 2+2 coordinates. We therefore give two values for the expectation value of H and V in the table. The first ones are obtained using the wave function expressed in 3+1 coordinates. The second ones are based on 2+2 coordinates. Especially for H, we observe small deviations of the results that indicate that higher partial wave contributions are not completely negligible when small cutoffs R are used. The deviation of the binding energy and the expectation values is partly due to the missing angular momentum states but also due to the restriction to isospin $T = 0$ states. Generally, the wave function seems to be better represented in 3+1 coordinates. Nevertheless, even in 2+2 coordinates, the agreement of expectation values and binding energies is excellent. This is a nontrivial confirmation of our results. We note that the N^{4}LO results are the numerically most demanding ones since they required denser momentum grids and more partial waves for convergence. Finally, Table IV gives results for the point proton radii that, in our $T_4 = 0$ approximation, exactly agree with the point neutron radii. Again we find that there is no strict correlation of the radii and binding energies. The radii are remarkably independent of the cutoff parameter R. In the following section, we extend these calculations towards more complex systems using the no-core configuration interaction (NCCI) approach.

TABLE III. Calculated ^{4}He binding energies using chiral NN interactions at different orders of the chiral expansion and at five different values of R. Energies are given in MeV.

R [fm]	LO	NLO	N^{2}LO	N^{3}LO	N^{4}LO
^{4}He					
0.8	−50.14	−26.50	−26.68	−23.93	−23.43
0.9	−48.39	−27.52	−27.28	−23.93	−24.02
1.0	−45.46	−28.55	−28.13	−23.77	−24.29
1.1	−42.34	−29.72	−29.11	−23.73	−24.30
1.2	−39.43	−30.92	−30.16	−23.64	−24.13

B. No-core configuration interaction calculations

For larger nuclei, $A > 4$, we use NCCI methods to solve the many-body Schrödinger equation. These methods have advanced rapidly in recent years and one can now accurately solve fundamental problems in nuclear structure and reaction physics using realistic interactions; see, e.g., Ref. [84] and references therein. In this section we follow Refs. [85,86], where for a given interaction, we diagonalize the resulting many-body Hamiltonian in a sequence of truncated harmonic-oscillator (HO) basis spaces. The basis spaces are characterized by two parameters: $N_{\max}$ specifies the maximum number of total HO quanta beyond the HO Slater determinant with all nucleons occupying their lowest-allowed orbitals and $\hbar\omega$ specifies the HO energy. The goal is to achieve convergence as indicated by independence of these two basis parameters, either directly or by extrapolation [85,87–90].

TABLE IV. Binding energy E, expectation values of the Hamiltonian in 3+1 (2+2) coordinates $\langle H\rangle_1$ ($\langle H\rangle_2$), the kinetic energy $\langle T\rangle$, the potential energy in 3+1 (2+2) coordinates $\langle V\rangle_1$ ($\langle V\rangle_2$) for ^{4}He at order N^{4}LO. We also give results for the point proton rms radii r_p. Energies are given in MeV and radii in fm.

R [fm]	E	$\langle H\rangle_1$	$\langle H\rangle_2$	$\langle T\rangle$	$\langle V\rangle_1$	$\langle V\rangle_2$	r_p
0.8	−23.43	−23.39	−23.37	112.9	−136.2	−136.2	1.557
0.9	−24.02	−24.00	−23.99	101.4	−125.3	−125.3	1.545
1.0	−24.29	−24.27	−24.27	91.9	−116.1	−116.2	1.546
1.1	−24.30	−24.28	−24.29	83.7	−108.0	−108.0	1.554
1.2	−24.13	−24.11	−24.12	76.5	−100.6	−100.6	1.568
AV18	−24.25	−24.21	−24.16	97.7	−121.9	−121.9	1.515
CDBonn	−26.16	−26.08	−26.07	77.6	−103.6	−103.6	1.457
N^{2}LO [21]	−25.60	−25.58	−25.59	62.58	−88.16	−88.16	1.478
Idaho N^{3}LO [20]	−25.38	−25.37	−25.37	69.18	−94.55	−94.55	1.518

To improve the convergence behavior of the many-body calculations we employ a consistent unitary transformation of the chiral Hamiltonians. Specifically, we use the Similarity Renormalization Group (SRG) [91–94] approach that provides a straightforward and flexible framework for consistently evolving (softening) the Hamiltonian and other operators, including three-nucleon interactions [95–98]. In particular, at N^{3}LO and N^{4}LO this additional "softening" of the chiral NN potential is necessary to obtain sufficiently converged results on current supercomputers.

In the SRG approach, the unitary transformation of an operator, e.g., the Hamiltonian, is formulated in terms of a flow equation,

$$\frac{d}{d\alpha}H_\alpha = [\eta_\alpha, H_\alpha], \tag{18}$$

with a continuous flow parameter α. The initial condition for the solution of this flow equation is given by the "bare" chiral Hamiltonian. The physics of the SRG evolution is governed by the anti-hermitian generator η_α. A specific form widely used in nuclear physics [94] is given by

$$\eta_\alpha = m_N^2[T_{\rm rel}, H_\alpha], \tag{19}$$

where m_N is the nucleon mass and $T_{\rm rel}$ is the intrinsic kinetic-energy operator

$$T_{\rm rel} \equiv \frac{2}{3}\left(\frac{(\vec{p}_{12})^2}{2\mu} + \frac{(\vec{p}_{13})^2}{2\mu} + \frac{(\vec{p}_{23})^2}{2\mu}\right), \tag{20}$$

where $\vec{p}_{ij} = (\vec{p}_i - \vec{p}_j)/2$ are relative momenta of the nucleons and $\mu = m/2$ is the reduced two-nucleon mass. This generator drives the Hamiltonian towards a diagonal form in a basis of eigenstates of the intrinsic kinetic energy, i.e., towards a diagonal in momentum space.

Along with the reduction in the coupling of low-momentum and high-momentum components by the Hamiltonian, the SRG induces many-body operators beyond the particle rank of the initial Hamiltonian. In principle, all induced terms up to the A-body level should be retained to ensure that the transformation is unitary and the spectrum of the Hamiltonian is independent of the flow parameter. Here, we truncate the evolution at the three-nucleon level, neglecting four- and higher multinucleon induced interactions, which formally violates unitarity. For consistency, we check that for $A = 3$ we recover the exact results (for a given input potential); and for $A \geqslant 4$ we perform our calculations at two different values of α and compare our results with calculations without SRG evolution.

The flow equation for the three-body system is solved using a HO Jacobi-coordinate basis [98]. The intermediate sums in the three-body Jacobi basis are truncated at $N_{\rm max} = 40$ for channels with $J \leqslant 7/2$, $N_{\rm max} = 38$ for $J = 9/2$, and $N_{\rm max} = 36$ for $J \geqslant 11/2$. The SRG evolution and subsequent transformation to single-particle coordinates were performed on a single node using an efficient OpenMP parallelized code.

For the NCCI calculations we employ the code MFDn [99,100], which is highly optimized for parallel computing on current high-performance computing platforms. The size of the largest feasible basis space is constrained by the total number of three-body matrix elements required as input, as well as by the number of many-body matrix elements that are computed and stored for the iterative Lanczos diagonalization procedure. We can perform ^{4}He calculations up to $N_{\rm max} = 14$ with 3N interactions, but calculations of $A = 6$ and 7 nuclei are restricted to $N_{\rm max} = 12$, and for $A > 10$ we can only go up to $N_{\rm max} = 8$ with (induced) 3N interactions. Note that with bare NN interactions, i.e., without the SRG evolution and the induced 3N terms, we can go to significantly larger basis spaces, namely $N_{\rm max} = 20$ for ^{4}He; $N_{\rm max} = 18$ for $A = 6$; $N_{\rm max} = 16$ for $A = 7$; $N_{\rm max} = 14$ for $A = 8$; $N_{\rm max} = 12$ for $A = 9$ and 10; and $N_{\rm max} = 10$ for $A = 16$. The larger basis spaces achievable with NN-only interactions arise due to the significantly smaller memory footprint of the input Hamiltonian matrix element files and the smaller memory footprint of the many-body Hamiltonian itself which is stored completely in our calculations. The latter issue has been reported as approximately a factor of 40 reduction in memory footprint with NN-only interactions compared to NN+3N interactions [101]. The many-body calculations were performed on the Cray XC30 Edison at NERSC and the IBM BG/Q Mira at Argonne National Laboratory.

Finally, compared to the few-body bound state calculations presented above, we use the following simplifications in our many-body calculations: we employ the same (average) nucleon mass for the protons and the neutrons, $m_N = 938.92$ MeV. Also, we do add the two-body Coulomb potential between (pointlike) protons, but we do not take any higher-order electromagnetic effects into account. Furthermore, here

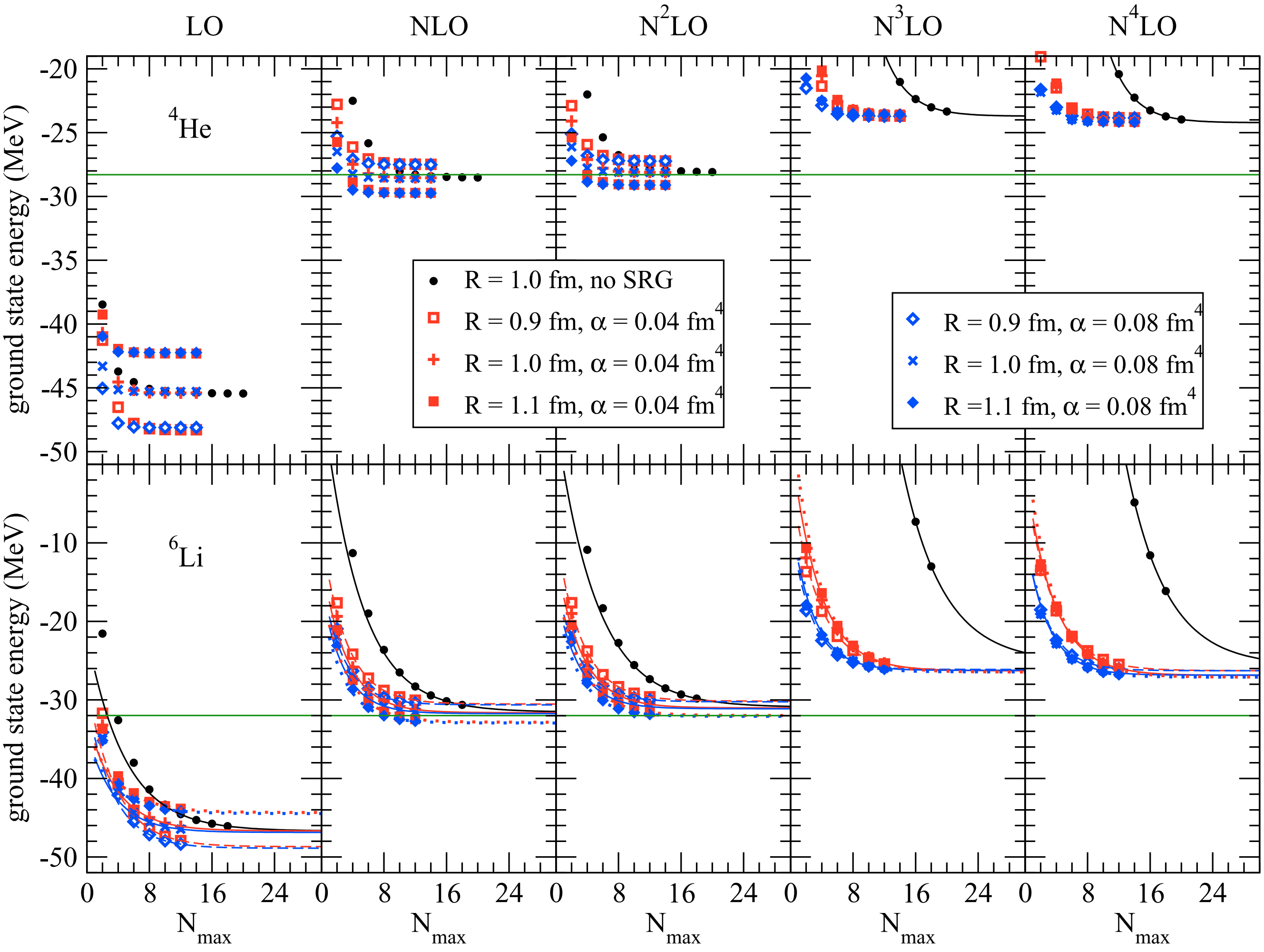

FIG. 10. Ground-state energies of ^{4}He and ^{6}Li at or just above the variational minimum in $\hbar\omega$ as a function of the basis truncation parameter N_{max} for LO to N^{4}LO chiral NN potentials: without SRG evolution (black dots) at $R = 1.0$ fm; and for NN potentials at $R = 0.9$ fm (open squares and open diamonds), $R = 1.0$ fm (plusses and crosses), and $R = 1.1$ fm (solid squares and solid diamonds), SRG evolved to 0.04 fm^4 (red) and 0.08 fm^4 (blue), including induced 3NF. Dotted ($R = 1.1$ fm), solid ($R = 1.0$ fm), and dashed ($R = 0.9$ fm) lines are exponential fits to the highest three N_{max} points for cases where convergence is not well-established by direct calculation.

and in what follows we restrict ourselves to the intermediate values of the coordinate-space regulator of $R = 0.9$, 1.0 and 1.1 fm. The smallest available cutoff choice of $R = 0.8$ fm leads to highly nonperturbative NN potentials [25,83], which cannot be employed in many-body calculations without SRG evolution or similar softening approaches. However, the softest regulator choice of $R = 1.2$ fm is known to lead to large finite-regulator artifacts [13,37,38], and for this reason we do not consider it in the following calculations.

C. Results for ground-state energies

In Fig. 10 we show our results for the ground-state energies of ^{4}He and ^{6}Li at LO to N^{4}LO, both without SRG evolution (for $R = 1.0$ fm only) and with SRG evolution (for $R =$ 0.9, 1.0, and 1.1 fm), including the induced 3N terms as mentioned above. (Note that, starting at N^{2}LO, there are also 3NFs in the chiral expansion, which are not incorporated in the calculations presented here.) Before examining these results in detail, we first make several qualitative observations: (1) The overall trends are the same for the different chiral cutoffs: significant overbinding at LO, close to the experimental values at NLO and N^{2}LO, and underbinding at N^{3}LO and N^{4}LO. (2) The dependence on the chiral cutoff R decreases with increasing chiral order, as expected. (3) The convergence rate changes dramatically with the chiral order – in particular when going from N^{2}LO to N^{3}LO, as anticipated by the Weinberg eigenvalue analysis of Ref. [83]. However, after applying the SRG evolution, convergence is reasonable, and the dependence of the converged energies on the SRG parameter α is negligible on the scale of these plots.

Based on the results in finite basis spaces, we can use extrapolations to the complete (infinite-dimensional) basis. Here we use a three parameter fit at fixed $\hbar\omega$ at or just above the variational minimum

$$E(N_{\text{max}}) \approx E_\infty + a\exp(-bN_{\text{max}}), \tag{21}$$

which seems to work well for a range of interactions and nuclei [85,86]. The lines in Fig. 10 correspond to the

TABLE V. Calculated ^{4}He and ^{6}Li ground-state energies (in MeV) using chiral NN interactions at three different values of R, SRG evolved to $\alpha = 0.04$ fm^4 (including induced 3NFs). The first theoretical error is the extrapolation uncertainty estimate following Ref. [86], whereas the second is an estimate of the SRG error, based on the difference between results at $\alpha = 0.04$ fm^4 and $\alpha = 0.08$ fm^4, due to omitting the induced multi-nucleon interactions at and above 4NFs.

R [fm]	LO	NLO	N^{2}LO	N^{3}LO	N^{4}LO
^{4}He					
0.9	$-48.284 \pm 0.002 \pm 0.17$	$-27.49 \pm 0.01 \pm 0.03$	$-27.23 \pm 0.01 \pm 0.01$	$-23.71 \pm 0.01 \pm 0.01$	$-23.85 \pm 0.01 \pm 0.01$
1.0	$-45.407 \pm 0.001 \pm 0.12$	$-28.542 \pm 0.004 \pm 0.03$	$-28.113 \pm 0.006 \pm 0.01$	$-23.59 \pm 0.01 \pm 0.01$	$-24.14 \pm 0.01 \pm 0.01$
1.1	$-42.312 \pm 0.001 \pm 0.07$	$-29.723 \pm 0.002 \pm 0.02$	$-29.102 \pm 0.003 \pm 0.01$	$-23.59 \pm 0.01 \pm 0.01$	$-24.18 \pm 0.01 \pm 0.01$
^{6}Li					
0.9	$-48.7 \pm 0.4 \pm 0.2$	$-30.5 \pm 0.1 \pm 0.1$	$-30.2 \pm 0.1 \pm 0.1$	$-26.2 \pm 0.2 \pm 0.1$	$-26.3 \pm 0.2 \pm 0.1$
1.0	$-46.7 \pm 0.3 \pm 0.2$	$-31.6 \pm 0.1 \pm 0.1$	$-31.0 \pm 0.1 \pm 0.1$	$-26.3 \pm 0.2 \pm 0.1$	$-26.9 \pm 0.3 \pm 0.1$
1.1	$-44.4 \pm 0.3 \pm 0.1$	$-32.8 \pm 0.1 \pm 0.1$	$-32.0 \pm 0.1 \pm 0.1$	$-26.4 \pm 0.2 \pm 0.1$	$-27.1 \pm 0.3 \pm 0.1$

extrapolating function fitted to the highest available $N_{\max}$ values. Our estimate of the extrapolation uncertainty is based on the difference with smaller $N_{\max}$ extrapolations, as well as the basis $\hbar\omega$ dependence over an 8 to 12 MeV span in $\hbar\omega$ values around the variational minimum [86]. As a consistency check, we first performed calculations for $A = 3$: including induced 3N contributions the results with and without SRG evolution are in agreement with each other, to within the estimated convergence or extrapolation uncertainty. Furthermore, they also agree with the Faddeev binding energies of Table I to within the estimated accuracy. Our results with SRG evolution to $\alpha = 0.04$ fm^4 for the ground-state energies of ^{4}He and ^{6}Li are summarized in Table V. In addition to the extrapolation uncertainty, we also give, as a second (systematic) contribution to the uncertainties, the difference between the ground-state energies at $\alpha = 0.04$ fm^4 and at $\alpha = 0.08$ fm^4, which may serve as an indication of the "error" made by neglecting induced many-body forces.

The ^{4}He results of Table V agree within the estimated uncertainties with the binding energies presented in Table III, at least at LO, NLO, and N^{2}LO. However, at N^{3}LO and N^{4}LO there are systematic differences: at N^{3}LO these differences are between 140 and 220 keV, depending on R, and at N^{4}LO between 120 and 170 keV. These differences are an order of magnitude larger than the estimated numerical uncertainties and are largest for $R = 0.9$ fm and smallest at $R = 1.1$ fm. That is, these difference are smallest for the softest interactions. A possible explanation for this discrepancy could be induced 4N forces, which we have neglected in the SRG evolution. This suggests that the difference between the ground-state energies

TABLE VI. Calculated ^{4}He, ^{6}Li, ^{10}B, and ^{16}O ground-state energies (in MeV) using chiral NN interactions at $R = 1.0$ fm without SRG evolution, and SRG evolved to $\alpha = 0.04$ fm^4 and $\alpha = 0.08$ fm^4 (including induced 3NFs). The theoretical error is the extrapolation uncertainty estimate following Ref. [86], adjusted to be at least 20% of the difference with the variational minimum.

α [fm^4]	LO	NLO	N^{2}LO	N^{3}LO	N^{4}LO
^{4}He, $J^P = 0^+$					
0	-45.453 ± 0.006	-28.533 ± 0.004	-28.11 ± 0.01	-23.7 ± 0.1	-24.2 ± 0.1
0.04	-45.407 ± 0.001	-28.542 ± 0.004	-28.113 ± 0.006	-23.59 ± 0.01	-24.14 ± 0.01
0.08	-45.289 ± 0.001	-28.566 ± 0.001	-28.119 ± 0.001	-23.582 ± 0.002	-24.145 ± 0.002
^{6}Li, $J^P = 1^+$					
0	-46.7 ± 0.1	-31.6 ± 0.2	-31.0 ± 0.2	-24.4 ± 2.3	-25.7 ± 1.9
0.04	-46.7 ± 0.3	-31.6 ± 0.1	-31.0 ± 0.1	-26.3 ± 0.2	-26.9 ± 0.3
0.08	-46.9 ± 0.3	-31.7 ± 0.1	-31.1 ± 0.1	-26.3 ± 0.2	-26.9 ± 0.3
^{10}B, $J^P = 1^+$					
0	-93.9 ± 0.8	-64.9 ± 1.8	-63.1 ± 1.9		
0.04	-94.0 ± 1.5	-64.5 ± 0.8	-63.1 ± 0.8	-55 ± 2	-55 ± 2
0.08	-94.9 ± 0.9	-64.3 ± 0.8	-63.1 ± 0.6	-52.2 ± 0.8	-53.3 ± 0.7
^{10}B, $J^P = 3^+$					
0	-88.1 ± 1.2	-64.6 ± 1.5	-62.3 ± 1.7		
0.04	-88.2 ± 1.6	-64.1 ± 0.7	-62.1 ± 0.8	-51 ± 4	-52 ± 3
0.08	-88.8 ± 1.0	-64.1 ± 0.6	-61.9 ± 0.6	-50.1 ± 1.0	-51.2 ± 0.9
^{16}O, $J^P = 0^+$					
0	-224 ± 2	-156 ± 5	-149 ± 5		
0.04	-223.2 ± 0.4	-152.0 ± 1.3	-146.2 ± 0.9	-121 ± 4	-121 ± 4
0.08	-220.9 ± 0.2	-150.1 ± 0.8	-144.8 ± 0.6	-113 ± 2	-114 ± 2

TABLE VII. Calculated NCCI ground state energies, in MeV, using chiral NN interactions at $R = 1.0$ fm (without SRG evolution). Results are compared with experimental data in the last column. The quoted theoretical errors are due to extrapolation uncertainties following Ref. [86], adjusted to be at least 20% of the difference with the variational minimum.

Nucleus	J^P	LO	NLO	N^{2}LO	Expt.
^{3}H	$\frac{1}{2}^+$	-11.30 ± 0.01	-8.38 ± 0.01	-8.28 ± 0.01	-8.482
^{4}He	0^+	-45.453 ± 0.006	-28.533 ± 0.004	-28.11 ± 0.01	-28.296
^{6}He	0^+	-43.2 ± 0.2	-28.7 ± 0.2	-27.9 ± 0.2	-29.27
^{6}Li	1^+	-46.7 ± 0.1	-31.6 ± 0.2	-31.0 ± 0.2	-31.99
^{7}Li	$\frac{3}{2}^-$	-57.1 ± 0.2	-38.7 ± 0.3	-38.0 ± 0.4	-39.24
^{8}He	0^+	-39.8 ± 0.6	-29.7 ± 0.5	-27.8 ± 0.6	-31.41
^{8}Li	2^+	-55.7 ± 0.5	-40.3 ± 0.7	-39.0 ± 0.8	-41.28
^{8}Be	0^+	-87.7 ± 0.4	-56.0 ± 0.7	-55.4 ± 0.9	-56.50
^{9}Li	$\frac{3}{2}^-$	-57.1 ± 0.4	-43.9 ± 0.7	-41.7 ± 0.8	-45.34
^{9}Be	$\frac{3}{2}^-$	-84.7 ± 0.7	-58.0 ± 1.4	-56.4 ± 1.5	-58.16
^{10}B	1^+	-93.9 ± 0.8	-64.9 ± 1.8	-63.1 ± 1.9	-64.03
^{10}B	3^+	-88.1 ± 1.2	-64.6 ± 1.5	-62.3 ± 1.7	-64.75
^{16}O	0^+	-224 ± 2	-156 ± 5	-149 ± 5	-127.62

at $\alpha = 0.04$ fm^4 and at $\alpha = 0.08$ fm^4, may indeed serve as an indication of the "error" made by neglecting induced many-body forces up to N^{2}LO, but is likely to underestimate the effect of neglected many-body forces at N^{3}LO and N^{4}LO. Note that without the SRG evolution the many-body calculation of the binding energy does agree with the Yakubovsky calculation, though the extrapolation uncertainty is significantly larger; see Table VI below.

As already mentioned, at LO we find considerable overbinding for all three values of the chiral cutoff R. This overbinding depends significantly on R and is strongest for $R = 0.9$ fm. At NLO (and N^{2}LO), the R-dependence is reduced by a factor of about two to three. Furthermore, the pattern is reversed compared to the LO results: At NLO and N^{2}LO, $R = 0.9$ fm leads to a slight underbinding, whereas $R = 1.1$ fm gives slight overbinding for ^{4}He and ^{6}Li. At N^{3}LO the R-dependence is further reduced by about an order of magnitude compared to NLO and N^{2}LO, and for ^{6}Li becomes of the same order as the many-body extrapolation uncertainty. Interestingly, at LO in the chiral expansion, ^{6}Li is not actually bound with respect to the $\alpha + d$ breakup, whereas at NLO and N^{2}LO it is bound by about 0.7 to 0.9 MeV (and it appears to remain bound at higher orders as well).

In Table VI we summarize our results with and without SRG evolution for several representative p-shell nuclei at LO through N^{4}LO for $R = 1.0$ fm. The errors listed in Table VI are our estimates of the extrapolation uncertainties, adjusted to be at least 20% of the difference with the variational minimum. Again, induced 3N contributions to the SRG-evolved interaction are included, but induced 4N and higher multi-nucleon induced interactions neglected. The differences between results without SRG evolution and at SRG values of $\alpha = 0.04$ fm^4 and at $\alpha = 0.08$ fm^4 tend to be of the same order as (or smaller than) the extrapolation uncertainties, except at leading order. When compared with the results at $\alpha = 0.04$ fm^4, the results at $\alpha = 0.08$ fm^4 generally do have smaller extrapolation uncertainties (i.e., are more converged in the many-body basis expansion) as one would expect, but are slightly further away from the results without SRG renormalization, where available.

At N^{3}LO and N^{4}LO, we have to rely on SRG evolution (or other renormalization schemes) for p-shell nuclei. For ^{6}Li we can do an extrapolation of the bare interaction results, but the extrapolation uncertainty is large, whereas the results at $\alpha = 0.04$ fm^4 and $\alpha = 0.08$ fm^4 differ by less than 100 keV. For the upper half of the p-shell, SRG evolution also becomes beneficial at NLO and N^{2}LO.

In Table VII and Fig. 11 we summarize our results for the ground-state energies of $A = 3$ to $A = 16$ nuclei based on extrapolations of the chiral LO, NLO, and N^{2}LO interactions without applying any further SRG renormalization. With the exception of ^{7}Li at LO, and of ^{10}B, the ground-state spins all agree with the experimental spin of the ground state. The results with SRG evolution, through the limited range that we investigate, (including induced 3NFs) are very similar, and fall within the quoted uncertainty estimates for all cases. Given this similarity of results with and without SRG evolution we do not present here the results with SRG evolution.

The ground-state energies of all nuclei in Table VII follow similar patterns: significantly overbound at LO, closer to the experimental values at NLO, and then shifted towards less binding at N^{2}LO. E.g., the $J^\pi = \frac{3}{2}^-$ ground state of ^{7}Li follows the same overall pattern as that of ^{4}He and ^{3}H, and is actually bound with respect to breakup into ^{4}He plus ^{3}H at LO, NLO and N^{2}LO. However, at $A = 8$ (and to a lesser extend also at $A = 9$) we see that the difference between LO and NLO results decreases significantly with increasing isospin: it is much smaller for the ^{8}He than it is for ^{8}Be. Also note that the deviation from experiment at N^{2}LO is largest for ^{8}He, and smallest for ^{8}Be. (Similar effects can be seen for ^{9}Li and ^{9}Be.) Neither ^{8}He nor ^{8}Be are bound at LO (^{8}He is about 5.5 MeV above ^{4}He, and ^{8}Be is about 3.3 MeV above two α-particles, and the applicability of the HO basis is rather questionable for these states). However, at NLO ^{8}He does become bound, whereas ^{8}Be remains unbound, both in qualitative agreement with experiment. Whether or not ^{6}He (and ^{8}He) are bound

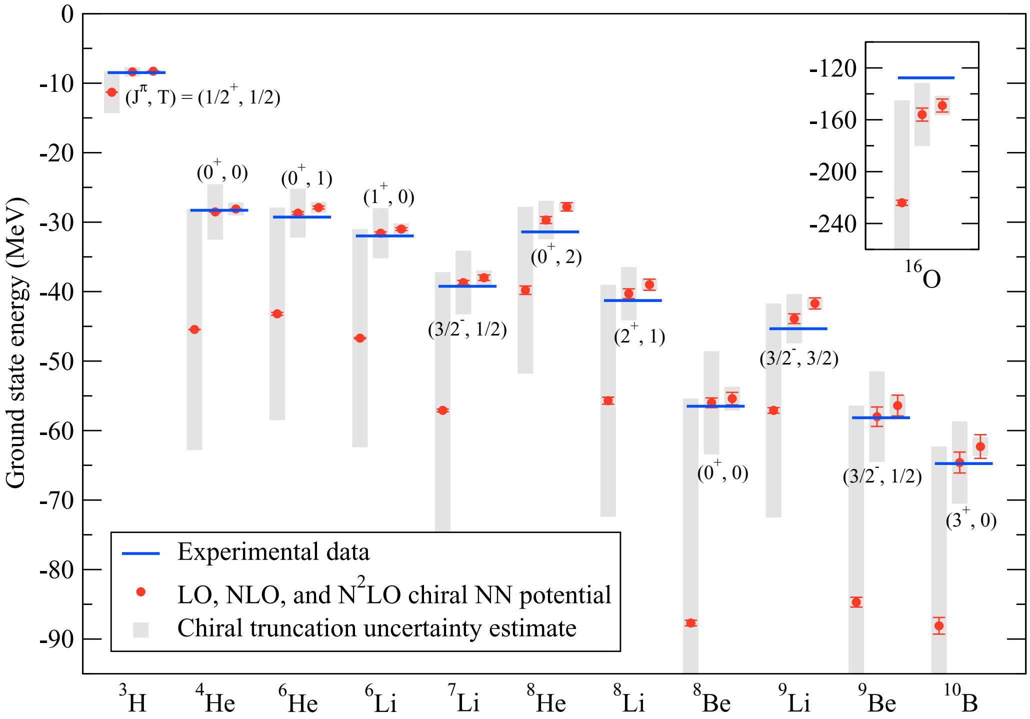

FIG. 11. Calculated (red dots) ground-state energies in MeV using chiral LO, NLO, and N^{2}LO NN interactions at $R = 1.0$ fm (without SRG evolution) based on the NN forces only in comparison with experimental values (blue levels). Red error bars indicate NCCI extrapolation uncertainty and shaded bars indicate the estimated truncation error at each chiral order as defined in the Introduction.

at N^{2}LO (and higher orders) depends crucially on the chiral 3NFs – without these, they are not bound. Note that ^{9}Be is also not bound at LO: despite the enormous overbinding compared to experiment, it is not bound with respect to breakup into two α-particles plus a neutron, and its ground-state energy is even above that of ^{8}Be. Only at NLO does ^{9}Be become bound and it may remain bound at N^{2}LO but the uncertainties do not allow us to make a definite statement.

Finally, the level ordering of the lowest states of ^{10}B is known to be sensitive to the details of the interaction [102], and typically one finds a $J^\pi = 1^+$ ground state with NN-only potentials, instead of a 3^+ ground state. With a 3NF one can obtain the correct $J^\pi = 3^+$ ground-state spin for ^{10}B, but the convergence pattern of the lowest 1^+ is different than that of the lowest 3^+ state; furthermore, the splitting between these two states appears to be very sensitive both to the parameters of the interaction and to the SRG evolution [97]. In our calculations, the 1^+ is the ground state at LO, and about 6 MeV below the 3^+ state, but at NLO and at N^{2}LO the level splitting between these two states is less than our estimated extrapolation uncertainties.

We show the chiral truncation error estimate for the ground-state energies of light nuclei up to $A = 10$ using the methods reviewed in Sec. I but limited to N^{2}LO in Fig. 11. We remind the reader that the shown results at N^{2}LO are incomplete as the corresponding 3NF are not included. Accordingly, at leading order, the chiral error estimate appears to be given by $\delta E^{(0)} = |E^{(3)} - E^{(0)}|$, and at NLO and N^{2}LO by $Q\delta E^{(0)}$ and $Q^2\delta E^{(0)}$, respectively, for all 10 nuclei. As in Ref. [43], the expansion parameter for these light nuclei is estimated here as $Q = M_\pi/\Lambda_b$ (see Sec. IV C). Note that if we were to include results up to N^{4}LO without including 3NFs (and possibly 4NFs), all chiral error estimates following this prescription would increase noticeably, because the N^{3}LO and N^{4}LO results without consistent 3NFs leads to a larger $\max(|E^{(i)} - E^{(0)}|)$ that appears in Eq. (6). Alternative chiral truncation error estimates for these results are discussed in Sec. V below.

Looking further into the results in Fig. 11, one notices that at N^{2}LO, where omitted 3NFs may have an impact, we see significant differences between the current results and experiment that go beyond the estimated chiral truncation uncertainty. These differences are easily visible for ^{6}He, ^{8}He, ^{8}Li, and ^{9}Li. Future work that includes the 3NFs is needed to discern their role and to understand if they resolve these differences while not creating significant differences in the cases where little difference is currently found.

D. Magnetic moments

In addition to binding energies we also calculated the magnetic moments for the ground states of p-shell nuclei up to $A = 10$. In contrast to long-range observables such as radii, magnetic moments tend to converge rapidly in a HO basis. Indeed, the magnetic moments for the ground states of ^{6}Li, ^{7}Li, and ^{7}Be are very well converged. Furthermore, the dependence on the chiral order is very weak, and the results are remarkably close to the experimental values. For $A = 8$ and 9, the convergence is not as good, and there is a stronger dependence on the chiral order, but the magnetic moment of the ground state of ^{10}B is again very well converged, and only very weakly dependent on the chiral order.

Note that here we only used the canonical one-body current operator and we defer to a future effort the development and application of consistent chiral current operators at each order. Our preliminary results with 3NFs at N^{2}LO indicate that the inclusion of consistent 3NFs at N^{2}LO does not change the magnetic moments significantly. We expect that with such improved current operators, including meson-exchange currents [103–108], the calculated magnetic moments (as well as magnetic transition matrix elements) will be in good agreement with experimental values—the deviation with experimental magnetic moments that we find here are of the same sign and magnitude as suggested by phenomenological meson-exchange contributions [107].

IV. MEDIUM-MASS NUCLEI

Over the past few years, several *ab initio* methods have been developed to address ground states of nuclei in the medium-mass regime, beyond the reach of standard NCCI calculations. Already the simplest observables, like ground-state energies and radii for medium-mass nuclei, e.g., the doubly magic calcium isotopes, provide a valuable testing ground for chiral interactions, far away from the few-body domain that was used to constrain the Hamiltonians.

For a first characterization of the new generation of chiral NN interactions in the medium-mass regime, we employ the most advanced coupled-cluster (CC) formulations and state-of-the-art in-medium similarity renormalization group (IM-SRG) calculations for ground-state observables of ^{16,24}O and ^{40,48}Ca. We mirror the discussion of the previous section and analyze the order-by-order behavior and the theoretical uncertainties. In addition, we compare to results with other, widely used chiral forces.

A. Coupled-cluster theory

Single-reference CC theory expresses the exact many-body state as $|\Psi\rangle = e^T|\Phi\rangle$, where $|\Phi\rangle$ is a single-Slater-determinant reference state based on a Hartree-Fock calculation [109–118]. Correlations are introduced by the action of the exponential e^T of the particle-hole excitation operator $T = T_1 + T_2 + \cdots + T_A$ on the reference state. In practical calculations, the cluster operator T is truncated at some low n-particle-n-hole (npnh) excitation level, such as the 2p2h excitations, $T \approx T_1 + T_2$. This constitutes the very popular CC with singles and doubles excitations (CCSD) approach. Due to the exponential ansatz, all powers of T_1, T_2 and mixed products of these are present in the description of the wave function, resulting in the facility to describe many-body correlations of considerable complexity that may be difficult to achieve in alternative many-body methods.

The essential ingredient in CC theory is the similarity-transformed Hamiltonian $\bar{H} = e^{-T}He^T$. In terms of $\bar{H}$, one can solve for the T amplitudes by projecting from the left with particle-hole excited reference states $|\Phi_{ij\ldots}^{ab\ldots}\rangle$ to obtain the set of equations $0 = \langle\Phi_{ij\ldots}^{ab\ldots}|\bar{H}|\Phi\rangle$ which determines the cluster amplitudes. The energy is obtained from calculating the closed diagrams of $\bar{H}$ according to $E = \langle\Phi|\bar{H}|\Phi\rangle$ [119].

Going beyond the singles and doubles approximation in CC calculations leads to an increased complexity of the equations to be solved and to increased computational cost. Therefore, the current approach in nuclear structure theory to incorporate higher-than-doubles excitations in ground-state CC calculations is by a noniterative inclusion of triples excitation effects to the ground-state energy (but not the wave function) via the CCSD(T) [120], ΛCCSD(T) [121,122], or the CR-CC(2,3) [123] method.

Three-body interactions can be included in CC calculations using the normal-ordering approximation at the two-body level (NO2B) [109,124]. Alternatively, the CC method can straightforwardly be extended to the full treatment of three-body Hamiltonians, however, often at prohibitively large computational cost [111,113]. In this work, we will work with the CCSD approach combined with the CR-CC(2,3) energy correction including 3N interactions in the NO2B approximation.

B. In-medium similarity renormalization group

The IM-SRG aims at decoupling an A-body reference state $|\Phi\rangle$ from all particle-hole excitations or, equivalently, at suppressing a specific "off-diagonal" part of the Hamiltonian [125–128]. This decoupling at the A-body level can be implemented using the concepts of the similarity renormalization group, that we already exploited in few-body spaces (cf. Sec. III B). We formulate a continuous unitary transformation of the Hamiltonian $H(s) = U^\dagger(s)H(0)U(s)$ in A-body space, where s denotes the flow parameter of the IM-SRG. This transformation is rewritten into the following operator differential equation:

$$\frac{dH}{ds}(s) = [\eta(s)\,, H(s)], \tag{22}$$

where $\eta(s)$ refers to the so-called generator of the transformation. The Hamiltonian $H(s)$ and the generator $\eta(s)$ are normal-ordered with respect to the reference state $|\Phi\rangle$ and truncated at the normal-ordered two-body level, e.g.,

$$\begin{aligned} H(s) = E(s) + \sum_{pq} f_q^p(s)\{a_p^\dagger a_q\} \\ + \frac{1}{4}\sum_{pqrs}\Gamma_{rs}^{pq}(s)\{a_p^\dagger a_q^\dagger a_r a_s\}, \end{aligned} \tag{23}$$

where normal-ordered products of single-particle creation and annihilation operators appear. Evaluating the right-hand side of Eq. (22) via Wick's theorem, one can derive the flow equations for the matrix elements of the normal-ordered zero-, one-, and two-body part, i.e., $E(s)$, $f_q^p(s)$, and $\Gamma_{rs}^{pq}(s)$, respectively, of the Hamiltonian. As an example, the flow equation for zero-body part, which represents energy expectation value in the reference state, reads

$$\begin{aligned} \frac{dE(s)}{ds} = \sum_{pq}(n_p - n_q)\,\eta_q^p(s)\,f_p^q(s) + \frac{1}{4}\sum_{pqrs}\big(\eta_{rs}^{pq}(s) \\ \times \Gamma_{pq}^{rs}(s)\,n_p n_q(1-n_r)(1-n_s) - [\eta\leftrightarrow\Gamma]\big), \end{aligned} \tag{24}$$

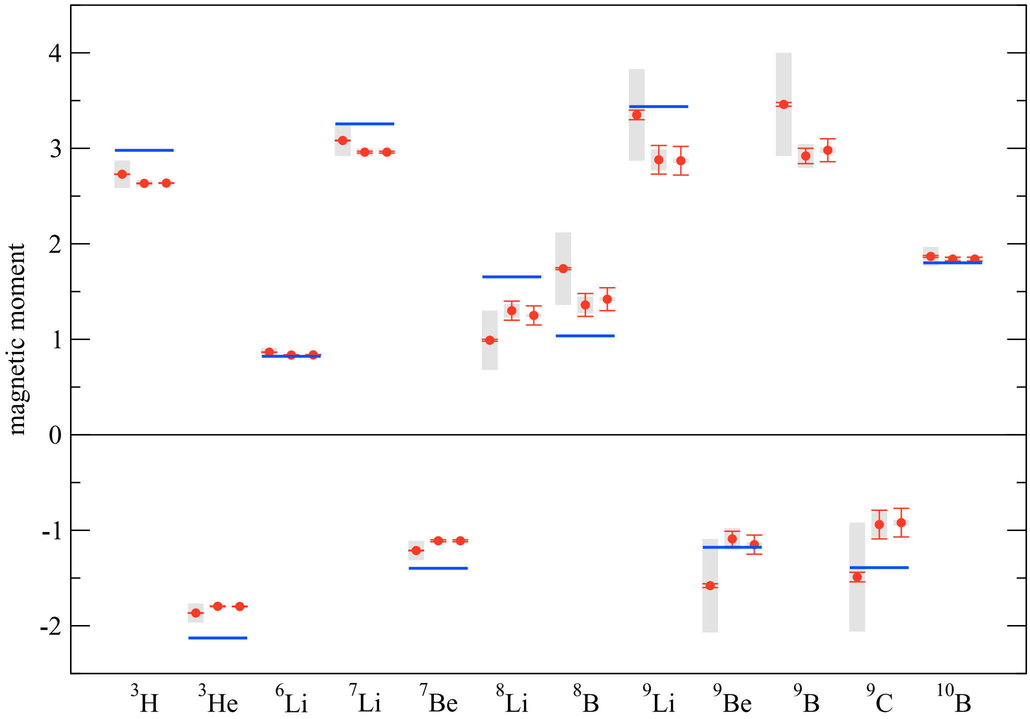

FIG. 12. Calculated (red dots) ground-state magnetic moments of light nuclei up to $A = 10$ at LO, NLO, and N^{2}LO with $R = 1.0$ fm in comparison with experimental values (blue horizontal lines). Red error bars indicate NCCI extrapolation uncertainty and shaded bars indicate the estimated truncation error at each chiral order as defined in the Introduction.

where n_p is the occupation number w.r.t. the reference state $|\Phi\rangle$. Formally, the flow equations of the IM-SRG are a coupled system of first-order ordinary differential equations which can be solved numerically as an initial value problem until decoupling is reached.

A great advantage of the IM-SRG is the simplicity and flexibility of its basic concept. Through different choices for the generator $\eta(s)$, we obtain different decoupling patterns, numerical characteristics and efficiencies. As a consequence, we can tailor the IM-SRG for specific applications, e.g., the derivation of valence-space shell model interactions [129–131]. Furthermore, it is straightforward to use the formalism of the IM-SRG for a consistent evolution of observables since the flow equation for an observable is similar to the one given in Eq. (22). The IM-SRG was first applied for the study of ground-state energies of closed-shell nuclei but can be easily extended to open-shell nuclei via multi-reference generalizations of normal ordering and Wick's theorem [132–134].

C. Chiral truncation error

To quantify the truncation errors in nuclear ground-state energies at various chiral orders, we recall the approach introduced in Ref. [43], see the discussion in Sec. I, and employ Eqs. (5) and (6) at LO and NLO and Eq. (8) at N^{2}LO and higher chiral orders. In Ref. [43], the expansion parameter Q of the chiral expansion defined in Eq. (7), which enters Eqs. (5), (6), and (8), was estimated for ^{3}H, ^{4}He, and ^{6}Li as $Q = M_\pi/\Lambda_b$. While this is reasonable for very light nuclei as seen in the discussion of chiral truncation errors in light nuclei in Sec. III, one may expect the typical momentum to increase in heavier systems due to the increased role of Pauli blocking.

To estimate these effects, we employ two different methods to evaluate a nucleus-dependent characteristic momentum scale: the Hartree-Fock (HF) approximation and the NCCI method. We use the resulting ground-state wave function, in each case, to evaluate the expectation value of the relative kinetic energy operator $\langle T_{\rm rel}\rangle$ given by

$$T_{\rm rel} \equiv \sum_{i<j} \frac{(\vec{p}_i - \vec{p}_j)^2}{2\,A\,m} = \frac{2}{A} \sum_{i<j} \frac{(\vec{p}_{ij})^2}{2\,\mu}, \qquad (25)$$

in terms of the relative momenta $\vec{p}_{ij} = (\vec{p}_i - \vec{p}_j)/2$ and the reduced two-nucleon mass $\mu = m/2$. Based on this expectation value, we define the average relative momentum scale as follows:

$$p_{\rm avg} = \sqrt{\frac{2\mu}{(A-1)}\langle T_{\rm rel}\rangle} = \sqrt{\frac{2}{A(A-1)}\left\langle \sum_{i<j} (\vec{p}_{ij})^2 \right\rangle}. \qquad (26)$$

As the last expression shows, this simply corresponds to the root-mean-square relative momentum of all nucleon pairs, i.e., the square root of the expectation value of the squared relative momenta summed over all particle pairs and divided by the number of pairs. Thus, this quantity reflects a characteristic scale for relative two-body momenta in the nucleus, which will depend on the nucleus under consideration and on the underlying interaction.

The results for $p_{\rm avg}$ obtained in HF and NCCI are summarized by Tables X and XI in the appendix. For HF, we employ the SRG-evolved Hamiltonian with the SRG

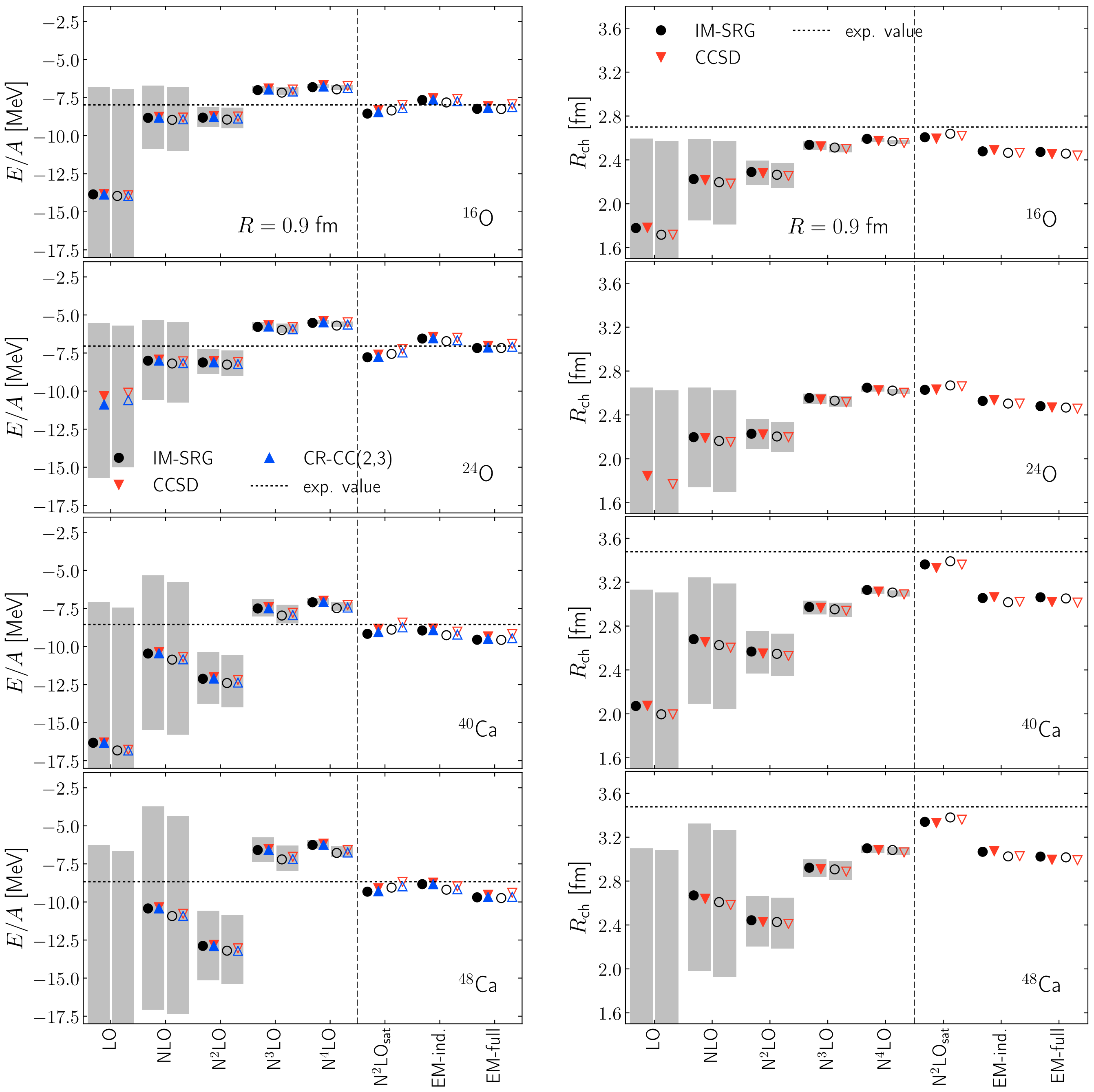

FIG. 13. Ground-state energies and charge radii for the ground state of ^{16,24}O and ^{40,48}Ca obtained from CC and IM-SRG based on HF reference states. The different columns correspond to different initial interactions, starting with the SCS chiral NN interaction from LO to N^{4}LO with the cutoff $R = 0.9$ fm, followed by the N^{2}LO-SAT NN+3N interaction [135], chiral NN interaction at N^{3}LO by Entem and Machleidt [20] without (EM-ind) and with (EM-full) an additional local chiral 3N interaction at N^{2}LO [136] with reduced cutoff $\Lambda_{3N} = 400$ MeV [124]. Solid symbols refer to a free-space SRG parameter $\alpha = 0.08$ fm^4 whereas open symbols refer to $\alpha = 0.04$ fm^4. The gray bars indicate the estimated theoretical uncertainties at various chiral orders.

parameter $\alpha = 0.08$ fm^4 and evaluate the expectation value of the SRG-transformed relative kinetic energy operator for input to the calculation of p_{avg}. We also employ the spherical HF approximation and the filling fraction approximation for open shell nuclei. For NCCI, we extrapolate the expectation value of the relative kinetic energy to the infinite basis limit using NCCI results from currently attainable $N_{\max}$ values.

The HF results are available for all chiral orders and show a systematic decrease in p_{avg} with increasing order. Pronounced changes appear from LO to NLO and from N^{2}LO to N^{3}LO. This general trend can be explained in a simple mean-field type picture, keeping the behavior of the ground-state charge radii in mind. With increasing chiral order the radius of a given nucleus shows a systematic increase (including the more pronounced

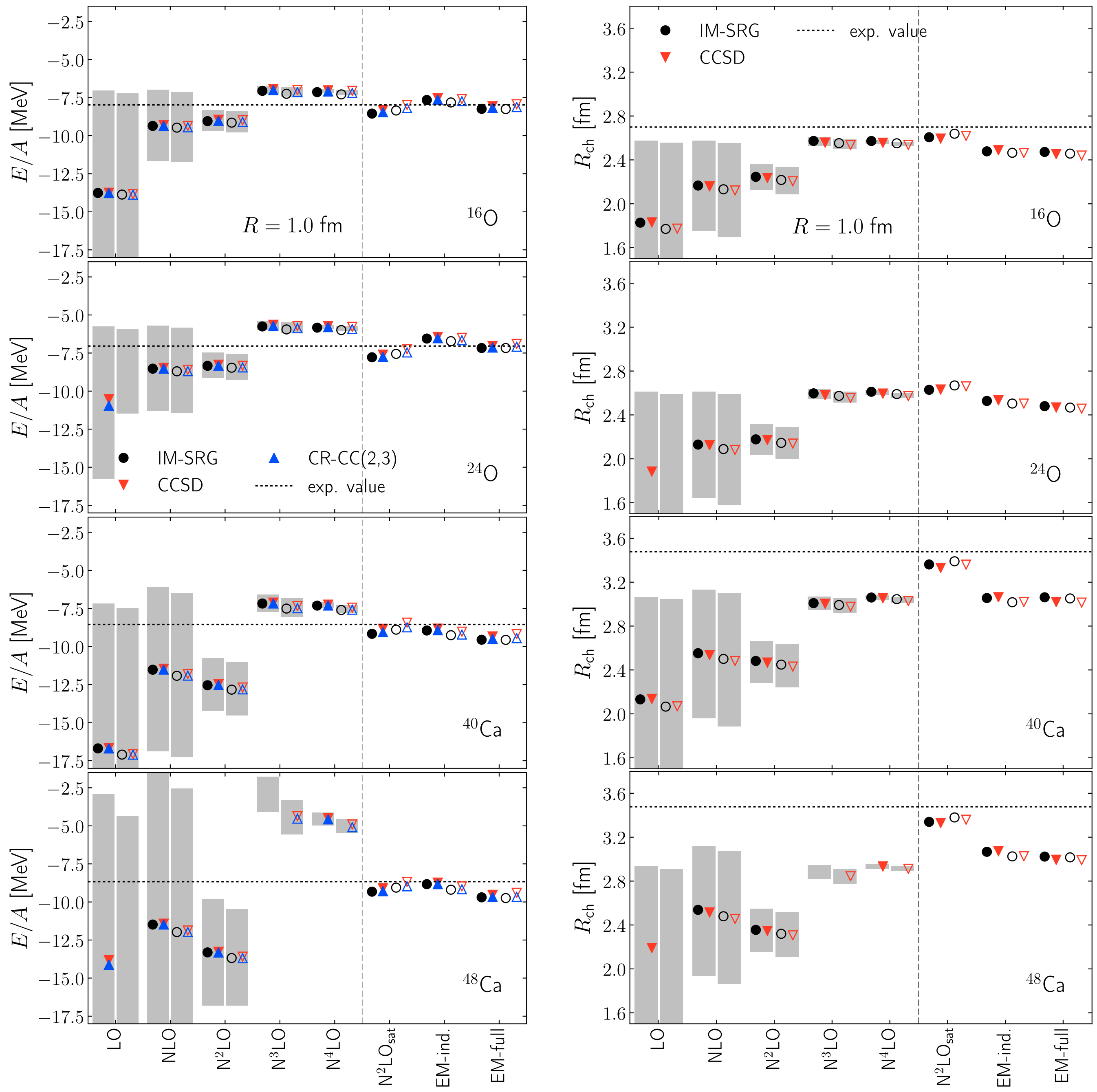

FIG. 14. Same as Figure 13 but for the cutoff value of $R = 1.0$ fm.

changes, cf. Figs. 13 and 14), which translates into a decrease of the Fermi energy and the associated momentum scale in a mean-field picture. The $p_{\rm avg}$ scale evaluated at the HF level captures exactly this mean-field or low-momentum physics.

It is interesting to compare this to the NCCI calculations, which converge to the exact solution of the many-body problem, including all correlations beyond the mean-field level. These results are available up to N^{2}LO for the p-shell nuclei and up to N^{4}LO for s-shell nuclei (both from Faddeev-Yakubovsky and NCCI calculations). Up to N^{2}LO the $p_{\rm avg}$ scales extracted from the NCCI kinetic energies for the bare Hamiltonian agree surprisingly well with scales extracted from HF expectation values based on SRG-evolved operators. This indicates the the SRG transformation does capture the main beyond-HF correlations such that the kinetic energy expectation values are very similar to the full NCCI values. Still, even with the SRG transformation, not all correlations are covered and the HF ground-state energies differ significantly from the converged NCCI result.

This difference becomes apparent at N^{3}LO and N^{4}LO, where the SCS NN interactions are significantly harder and much more difficult to converge in the NCCI than at lower orders (see, e.g., Fig. 10). This is the reason why no NCCI scales can be extracted for p-shell nuclei beyond N^{2}LO. For

TABLE VIII. Ground-state energies per nucleon, in MeV, using SRG-evolved SCS NN interactions from LO to N^{4}LO at $R = 0.9$ fm and $R = 1.0$ fm obtained form CCSD, CR-CC(2,3) and IM-SRG calculations. For each isotope, method and chiral truncation two numbers are given, where the first corresponds to an SRG-flow parameter $\alpha = 0.04\,\text{fm}^4$ and the second to $\alpha = 0.08\,\text{fm}^4$. If no result is quoted, then the CC or IM-SRG equations did not provide a stable solution, because the initial HF single-particle spectrum does not exhibit the correct shell closures.

Nucleus	Method	LO	NLO	N^{2}LO	N^{3}LO	N^{4}LO	Exp.
$R = 0.9$ fm							
^{16}O	CCSD	−13.92; −13.84	−8.81; −8.76	−8.74; −8.71	−6.97; −6.90	−6.74; −6.69	−7.98
	CR-CC(2,3)	−13.97; −13.86	−8.93; −8.82	−8.88; −8.79	−7.10; −6.97	−6.87; −6.77	
	IM-SRG	−13.96; −13.86	−8.96; −8.83	−8.94; −8.82	−7.17; −7.01	−6.96; −6.81	
^{24}O	CCSD	−10.11; −10.33	−8.05; −7.93	−8.09; −8.03	−5.80; −5.68	−5.48; −5.40	−7.04
	CR-CC(2,3)	−10.59; −10.89	−8.17; −8.00	−8.23; −8.11	−5.94; −5.76	−5.63; −5.48	
	IM-SRG	—;—	−8.19; −8.00	−8.26; −8.12	−5.99; −5.78	−5.70; −5.52	
^{40}Ca	CCSD	−16.78; −16.30	−10.69; −10.37	−12.19; −12.01	−7.79; −7.42	−7.27; −6.99	−8.55
	CR-CC(2,3)	−16.83; −16.33	−10.84; −10.44	−12.37; −12.10	−7.94; −7.49	−7.44; −7.07	
	IM-SRG	−16.82; −16.32	−10.86; −10.46	−12.40; −12.12	−7.96; −7.50	−7.48; −7.09	
^{48}Ca	CCSD	—; —	−10.77; −10.35	−13.05; −12.82	−7.03; −6.52	−6.59; −6.17	−8.67
	CR-CC(2,3)	—; —	−10.92; −10.42	−13.21; −12.89	−7.19; −6.59	−6.75; −6.25	
	IM-SRG	—; —	−10.93; −10.43	−13.20; −12.89	−7.20; −6.59	−6.78; −6.26	
$R = 1.0$ fm							
^{16}O	CCSD	−13.84; −13.75	−9.36; −9.30	−8.98; −8.95	−7.00; −6.93	−7.06; −7.02	−7.98
	CR-CC(2,3)	−13.88; −13.77	−9.45; −9.36	−9.10; −9.02	−7.14; −7.01	−7.20; −7.10	
	IM-SRG	−13.87; −13.76	−9.47; −9.36	−9.15; −9.05	−7.25; −7.06	−7.29; −7.14	
^{24}O	CCSD	—; −10.53	−8.59; −8.47	−8.34; −8.27	−5.72; −5.64	−5.78; −5.72	−7.04
	CR-CC(2,3)	—; −10.97	−8.69; −8.53	−8.45; −8.33	−5.87; −5.72	−5.92; −5.80	
	IM-SRG	—; —	−8.70; −8.53	−8.46; −8.34	−5.95; −5.76	−5.99; −5.83	
^{40}Ca	CCSD	−17.07; −16.68	−11.81; −11.46	−12.69; −12.47	−7.34; −7.12	−7.45; −7.25	−8.55
	CR-CC(2,3)	−17.10; −16.69	−11.91; −11.52	−12.81; −12.53	−7.49; −7.18	−7.58; −7.31	
	IM-SRG	−17.10; −16.69	−11.92; −11.52	−12.83; −12.54	−7.51; −7.18	−7.60; −7.31	
^{48}Ca	CCSD	—; −13.82	−11.87; −11.42	−13.59; −13.27	−4.37; —	−4.91; −4.51	−8.67
	CR-CC(2,3)	—; −14.13	−11.98; −11.48	−13.70,; −13.32	−4.53; —	−5.10; −4.58	
	IM-SRG	—; —	−11.98; −11.48	−13.68; −13.31	—; —	—; —	

s-shell nuclei the p_{avg} scales obtained from NCCI at N^{3}LO and N^{4}LO are significantly larger than for the lower orders, in contrast to the mean-field trend shown by the HF-based scale estimates. At this point, short-range or high-momentum physics explicitly affects the momentum scales extracted from NCCI wave functions, which is absent in the HF treatment. Such short-range correlation effects are regulator scale and scheme dependent and represent specific high-momentum aspects of the wave function and not a gross momentum scale corresponding to the Fermi-momentum in a homogeneous system. We do not have a strong physics reason for preferring one or another approach to estimating the nucleus-dependent momentum scale p_{avg}. In the following, we adopt the HF-based scale estimate as input for the uncertainty quantification out of convenience.

Given that the p_{avg} values show significant variations at different chiral orders, we average over the available results from LO to N^{4}LO to arrive at a single nucleus-dependent and R-dependent value for p_{avg} quoted in the last column in Tables X and XI. Then, for a given nucleus, the expansion parameter Q is estimated as

$$Q = \frac{\max(p_{\text{avg}},\ M_\pi)}{\Lambda_b}, \tag{27}$$

where p_{avg} is the result in the last column of Tables X and XI.

Another feature of the results in Tables X and XI is the increase in p_{avg} with increasing A. For very heavy nuclei, the relevant momentum scale should be closer to the Fermi momentum $p_F \sim 260$ MeV corresponding to the saturation density of nuclear matter. The trend in the results of the last column of Tables X and XI appears consistent with that expectation. However, for light nuclei p_{avg} is within a few percent of of M_π, at least up to $A = 9$ for $R = 1.0$fm. Since the chiral uncertainty estimates shown in Figs. 11 and 12 would change only minimally by adopting p_{avg} for the definition of Q, we do not show them for light nuclei. However, for the following discussion of ground-state observables of medium-mass nuclei, we will adopt the nucleus-dependent momentum scales p_{avg} for the order-by-order uncertainty quantification. Furthermore, as already described in the previous sections, the considered properties of light nuclei based on NN interactions only tend to show significant jumps when going from N^{2}LO to N^{3}LO, which are probably artifacts of our calculations being incomplete and are expected to dissappear upon inclusion of the consistent 3N forces. To avoid overestimating the theoretical uncertainties, Eq. (6) is replaced in this paper by

$$\delta X^{(i)} \geqslant \max(|X^{(j\geqslant i)} - X^{(k\geqslant i)}|), \quad i, j, k \in \{0, 1, 2\}. \tag{28}$$

TABLE IX. Charge radii, in fm, using SRG-evolved SCS NN interactions from LO to N^{4}LO at $R = 0.9$ fm and $R = 1.0$ fm obtained form CCSD and IM-SRG calculations. For each isotope, method, and chiral truncation, two numbers are given, where the first corresponds to an SRG-flow parameter $\alpha = 0.04\,\text{fm}^4$ and the second to $\alpha = 0.08\,\text{fm}^4$. If no result is quoted, then the CC or IM-SRG equations did not provide a stable solution, because the initial HF single-particle spectrum does not exhibit the correct shell closures.

Nucleus	Method	LO	NLO	N^{2}LO	N^{3}LO	N^{4}LO	Exp.
$R = 0.9$ fm							
^{16}O	CCSD	1.72; 1.78	2.18; 2.22	2.25; 2.28	2.50; 2.52	2.55; 2.57	2.70
	IM-SRG	1.72; 1.78	2.20; 2.23	2.26; 2.29	2.51; 2.54	2.57; 2.59	
^{24}O	CCSD	1.77; 1.84	2.15; 2.19	2.20; 2.22	2.52; 2.54	2.60; 2.63	—
	IM-SRG	—; —	2.16; 2.20	2.20; 2.23	2.53; 2.55	2.62; 2.65	
^{40}Ca	CCSD	2.00; 2.07	2.60; 2.65	2.53; 2.55	2.94; 2.97	3.09; 3.11	3.48
	IM-SRG	2.00; 2.07	2.63; 2.68	2.55; 2.57	2.95; 2.97	3.11; 3.13	
^{48}Ca	CCSD	—; —	2.58; 2.64	2.41; 2.43	2.89; 2.91	3.06; 3.08	3.48
	IM-SRG	—; —	2.61; 2.67	2.43; 2.44	2.91; 2.92	3.08; 3.10	
$R = 1.0$ fm							
^{16}O	CCSD	1.77; 1.83	2.12; 2.16	2.21; 2.24	2.54; 2.56	2.54; 2.56	2.70
	IM-SRG	1.77; 1.83	2.13; 2.17	2.22; 2.25	2.55; 2.57	2.55; 2.57	
^{24}O	CCSD	—; 1.88	2.08; 2.12	2.14; 2.17	2.56; 2.58	2.57; 2.59	—
	IM-SRG	—; —	2.09; 2.13	2.15; 2.18	2.57; 2.60	2.59; 2.61	
^{40}Ca	CCSD	2.07; 2.14	2.48; 2.54	2.43; 2.47	2.98; 3.00	3.03; 3.05	3.48
	IM-SRG	2.07; 2.13	2.50; 2.55	2.45; 2.48	2.99; 3.01	3.04; 3.06	
^{48}Ca	CCSD	—; 2.19	2.46; 2.51	2.31; 2.35	2.84; —	2.91; 2.93	3.48
	IM-SRG	—; —	2.48; 2.54	2.32; 2.36	—; —	—; —	

D. Results

Using CC and IM-SRG we explore the ground-state energies and charge radii of the doubly magic nuclei ^{16,24}O and ^{40,48}Ca with the SCS NN interactions from LO to N^{4}LO. The focus of these calculations is the investigation of the order-by-order behavior of the chiral expansion in the medium-mass regime and the theory uncertainties derived from it.

For all calculations presented in this section we use SRG-evolved interactions including the induced three-nucleon contributions. We use two different SRG flow parameters, $\alpha = 0.04\,\text{fm}^4$ and $0.08\,\text{fm}^4$, to probe the contributions of higher-order induced forces that are not explicitly included. For the specific interaction and nucleus under consideration, we first perform a Hartree-Fock calculation for the full Hamiltonian in a HO basis truncated with respect to the maximum single-particle principal quantum number $e_{\max} = (2n + l)_{\max}$. The HF solution defines the reference state and an optimized single-particle basis, which eliminates the dependence of the subsequent many-body solutions on the oscillator frequency. The full Hamiltonian is normal-ordered with respect to the reference Slater determinant and residual normal-ordered three-body terms are discarded. We have explored the accuracy of the normal-ordered two-body approximation in the medium-mass regime, e.g., through direct comparisons of CC calculations with and without the residual three-body terms and found agreement at the 1% level or better [111,124].

With these inputs, we perform CC calculations at the level of CCSD and CR-CC(2,3), which provide a direct way to quantify the residual uncertainty due to the cluster truncation. In addition, we perform single-reference IM-SRG(2) calculations. The results for the ground-states energies and the charge radii of ^{16,24}O and ^{40,48}Ca are summarized in Fig. 13 for the sequence of SCS NN interaction at cutoff $R = 0.9$ fm and in Fig. 14 for $R = 1.0$ fm. For comparison each panel also shows the corresponding results with established chiral interactions, i.e., the N^{2}LO-sat NN+3N interaction by Ekström *et al.* [135], the N^{3}LO NN interaction by Entem and Machleidt [20] without (EM-ind) and with (EM-full) a supplementary local 3N interaction at N^{2}LO with cutoff 400 MeV [124,136]. The numerical values for the ground-state energies and charge radii obtained with the SCS NN interactions at cutoff values of $R = 0.9$ fm and $R = 1.0$ fm can be found in Tables VIII and IX, respectively.

The different symbol shapes and colors distinguish the three many-body methods while solid and open symbols indicate the two SRG flow-parameters we use. The variation within the set of six calculations for any given chiral interaction and nucleus provides an estimate for the uncertainties in the solution of the many-body problem, including the free-space SRG evolution and the many-body truncations.

These many-body uncertainties can be compared to the uncertainties inherent to the chiral interaction at any given order, which are quantified using the protocol discussed in Sec. IV C. We use the intrinsic kinetic energy expectation value obtained in HF calculations with SRG transformed operators to define a momentum scale. The uncertainties for the ground-state energies and the charge radii are then determined from Eqs. (5) and (28) for LO and NLO and Eq. (8) from N^{2}LO on. The gray bands in Figs. 13 and 14 indicate these uncertainties extracted from the IM-SRG results as representatives for the three different many-body approaches. For the neutron-rich isotopes ^{24}O and ^{48}Ca, the LO interaction does not reproduce the correct shell closures at the Hartree-Fock level and, thus, the closed-shell formulations of CC and IM-SRG typically fail to converge. In these cases we simply use the HF ground-state energy for the uncertainty quantification.

Generally we find a systematic decrease of the uncertainties with increasing chiral order, as expected. For the lower orders up to N^{2}LO, the interaction uncertainties are significantly larger than the many-body uncertainties. Only at N^{3}LO and N^{4}LO the interaction and many-body uncertainties are of comparable size. We conclude from this observation that the many-body methods and their truncation uncertainties are sufficiently well controlled to address nuclei in the medium-mass regime with chiral interactions. Even at the highest available order of the chiral expansion, the different sources of uncertainties are comparable in size, so that a significant improvement on the total uncertainty would require improvements on all aspects of the calculation.

The sequence of ground-state energies from LO to N^{4}LO for these medium-mass nuclei shows the same systematic pattern observed in light nuclei: The LO interactions for both cutoffs produce drastic overbinding and unrealistic ground states. Going to NLO the energy jumps and the overbinding is reduced significantly. The step to N^{2}LO does not affect the ground-state energies for the oxygen isotopes, but lowers the ground-state energies for the calcium isotopes again. Going to N^{3}LO the ground-state energies exhibit another jump leading to a moderate underbinding compared to experiment. From N^{3}LO to N^{4}LO the energies remain stable for all nuclei.

As repeatedly emphasized, one has to keep in mind that the 3N interactions, which appear from N^{2}LO on, are not included in these calculations. Therefore, we cannot draw rigorous conclusions about the convergence of the chiral expansion at this stage. It will be very interesting to explore how the inclusion of a consistent 3N interaction fitted in the few-body sector for N^{2}LO and beyond will change the observed trends in ground-state energies of medium-mass nuclei. This is the prime goal of our ongoing research program.

The charge radii mirror the pattern observed for the ground-state energies. As the ground-state energy increases and the binding decreases, the charge radii increase as expected from a naive mean-field picture. For N^{3}LO and N^{4}LO the charge radii for ^{16}O are close to the experimental value, however, for ^{40,48}Ca the radii are underestimated by about 0.4 fm although the nuclei are underbound. It remains to be seen, how the 3N contributions affect the radii, but it is unlikely that the inclusion of the consistent 3N interactions alone will resolve this discrepancy.

V. ALTERNATIVE APPROACHES FOR UNCERTAINTY QUANTIFICATION

As explained in the introduction, our simple and universal approach to estimating truncation errors assumes that the chiral expansion of the nuclear forces translates into a similar expansion for the calculated observables; see Eq. (4). While this assumption holds true for the scattering amplitude in a perturbative regime, it is violated in the near-threshold kinematics if the corresponding scattering lengths take large values [137], as is the case for the NN ^{1}S$_0$ and ^{3}S$_1$ partial waves. The large S-wave NN scattering lengths also result in the strong cancellations between the kinetic and potential energies when calculating the spectra of light nuclei [4]. Instead of trying to account for all relevant dynamically generated fine-tuned scales in all partial waves and for all kinematical conditions, we use a simplistic, universal approach to uncertainty quantification by incorporating the information about the actual pattern of the chiral expansion for a given observable to account for the above-mentioned departures from naive dimensional analysis. In the following, we address the reliability of the resulting error estimations, discuss the robustness of our approach and consider two alternative formulations.

Alternative approach 1

We first explore the possibility of relaxing the constraints in Eq. (28). To retain a realistic estimation of the truncation error especially at low orders of the chiral expansion, we still make use of the information about the explicit size of the order-Q^i contributions to an observable of interest for all available chiral orders. Specifically, we replace Eqs. (5) and (28) by

$$\delta X^{(0)} = \max_{i\geqslant 2}(Q^2|X^{(0)}|,\ Q^{2-i}|\Delta X^{(i)}|),$$
$$\delta X^{(j)} = Q^{j-1}\delta X^{(0)}, \quad \text{for } j \geqslant 2 \tag{29}$$

for the case of complete calculations. Such an approach may be expected to provide a more realistic estimation of uncertainties at lower orders in the chiral expansion as compared to the standard method. For incomplete calculations based on two-nucleon forces only, we rather estimate $\delta X^{(0)}$ via

$$\delta X^{(0)} = \max_{i\geqslant 3}(Q^2|X^{(0)}|, |\Delta X^{(2)}|, Q^{-1}|\Delta X^{(i)}|),$$
$$\delta X^{(j)} = Q^{j-1}\delta X^{(0)}, \quad \text{for } j \geqslant 2. \tag{30}$$

In practice, the above modifications are found to lead to very small changes in the estimated theoretical uncertainties. For example, using Eq. (29), we obtain for the neutron-proton total cross section at $E_{\text{lab}} = 143$MeV for the cutoff of $R = 0.9$ fm,

$$52.5 \pm 11.8_{[Q^0]} \rightarrow 49.1 \pm 5.1_{[Q^2]} \rightarrow 54.2 \pm 2.2_{[Q^3]} \rightarrow 53.7 \pm 1.0_{[Q^4]} \rightarrow 53.9 \pm 0.4_{[Q^5]}, \tag{31}$$

which has to be compared with the estimation based on the original approach using Eqs. (5) and (28):

$$52.5 \pm 9.8_{[Q^0]} \rightarrow 49.1 \pm 5.1_{[Q^2]} \rightarrow 54.2 \pm 2.2_{[Q^3]} \rightarrow 53.7 \pm 1.0_{[Q^4]} \rightarrow 53.9 \pm 0.4_{[Q^5]}. \tag{32}$$

Thus, in this particular case, the modification only amounts to a slight increase of the theoretical uncertainty at LO. Similarly, we find very minor changes when using Eq. (30) instead of Eq. (8) to estimate truncation errors in incomplete few-body calculations based on two-nucleon interactions only; see Fig. 15 for representative examples.

Alternative approach 2

Furthermore, we consider a minimalistic approach for uncertainty quantification of calculated ground-state

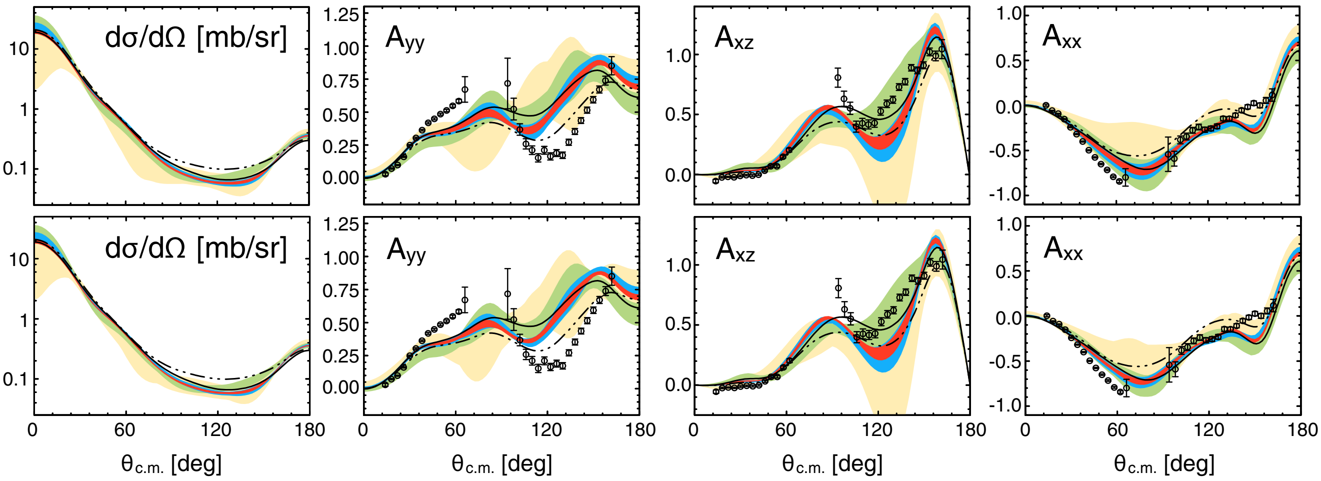

FIG. 15. Predictions for the differential cross section, and deuteron tensor analyzing powers A_{yy}, A_{xz}, and A_{xx} at the laboratory energy of 200 MeV based on the NN potentials of Refs. [13,14] for $R = 0.9$ fm without including the 3NF. The bands of increasing width show estimated theoretical uncertainty at N^{4}LO (red), N^{3}LO (blue), N^{2}LO (green), and NLO (yellow). The theoretical uncertainties in the upper and lower rows are estimated using Eq. (8) and (30), respectively. The dotted (dashed) lines show the results based on the CD Bonn NN potential (CD Bonn NN potential in combination with the Tucson-Melbourne 3NF). Open circles are proton-deuteron data from Refs. [138].

energies that does not rely on the knowledge of contributions beyond the leading order by assigning the uncertainties as

$$\delta E^{(0)} = Q^2 |\langle V\rangle^{(0)}|, \quad \delta E^{(i\geqslant 2)} = Q^{i+1} |\langle V\rangle^{(0)}|. \qquad (33)$$

without any further constraints. Also the momentum scale Q is based on the calculated p_{avg} at leading order given in Table X, whereas in the original approach and Alternative 1 we used the average of p_{avg} over all available chiral orders. Thus, the uncertainties are estimated entirely based on the leading order information.

Notice that using the expectation value of the potential energy rather than the binding energy as done in the original approach and Alternative 1 is crucial to account

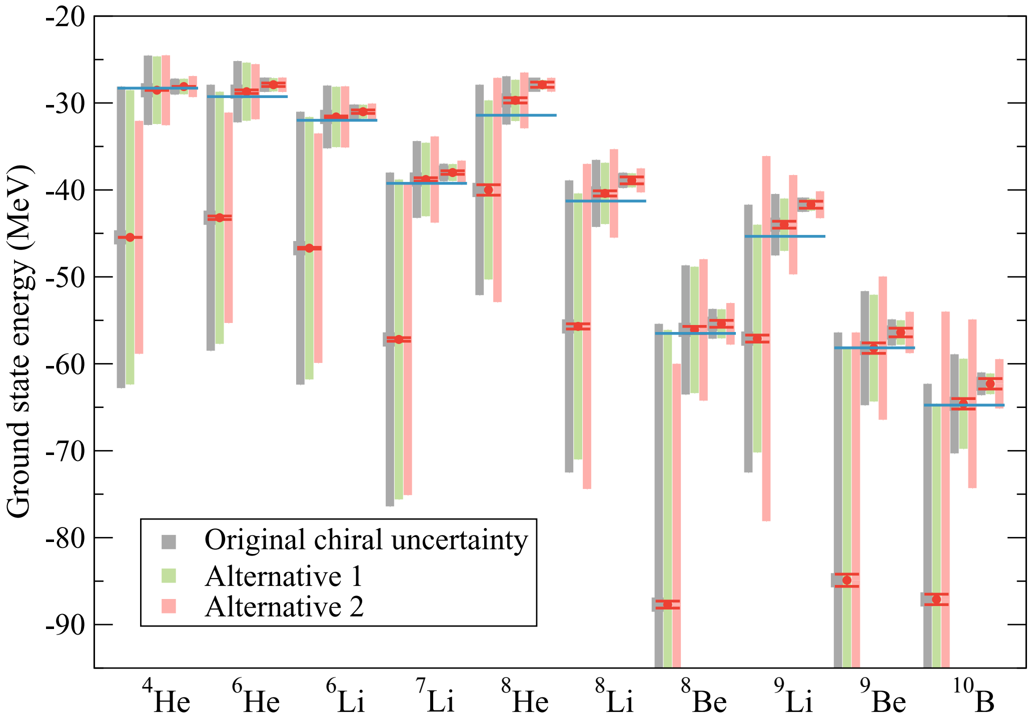

FIG. 16. Results from Fig. 11 showing chiral uncertainties as presented in the Introduction (gray bars) compared with the two alternative uncertainty estimates (green and pale red bars), discussed in the text. The red error bars indicate the many-body uncertainties. For comparison, the experimental ground-state energies are also shown as the blue bars.

for the fine-tuning associated with the NN interaction being close to the unitary limit (large S-wave scattering lengths). While the ignorance of the fine-tuned nature of the binding energies in the other two approaches is, to a large extent, effectively corrected by employing the available information about the actual pattern of the chiral expansion, an attempt to use the binding energy instead of $\langle V\rangle^{(0)}$ in Eq. (33) will yield drastically underestimated truncation errors.

This simple minimalistic approach has an appealing feature that the estimated uncertainties for the energies beyond the leading order do not involve any information on the specific behavior at higher orders as it only builds upon the expected suppression of higher-order contributions of the chiral EFT expansion. However, this method is less universal than the other two approaches since it is defined specifically for the bound state energy.

In Fig. 16 we show the results for light nuclei along with the uncertainty estimates presented in Fig. 11 and the uncertainty estimates from these alternative approaches. Overall, Alternative 1 produces very similar uncertainty estimates as the original approach for these calculations which are truncated at N^{2}LO, but there are some significant differences in the error estimates with Alternative 2. One of the most notable differences is for ^{10}B, where Alternative 2 produced the largest chiral uncertainty, and in general, Alternative 2 suggests larger chiral uncertainties than the original approach or Alternative 1 as A increases. Another significant difference is for $A = 8$ (^{8}He, ^{8}Li, and ^{8}Be), where the original error estimates increase significantly as one proceeds towards $N = Z$ at fixed A, but this does not happen as strongly with Alternative 2.

In Fig. 17 we show the results for ground-state energies per nucleon of light and medium nuclei with closed (sub)shells up to N^{4}LO with the different chiral error estimates. Overall, Alternative 2 produces very similar uncertainty estimates as the original approach for these calculations, but there are significant differences in the error estimates with Alternative 1. In particular, for the medium-mass nuclei ^{24}O, ^{40}Ca, and ^{48}Ca, Alternative 1 produces very large uncertainties at LO. This can be traced back to the large differences between the N^{2}LO results and N^{3}LO and N^{4}LO results for these nuclei. We emphasize, that the original error estimates and Alternative 1 are significantly influenced by the missing 3N (and possibly 4N) forces at N^{3}LO and N^{4}LO. Clearly the role of 3N (and possibly 4N) forces becomes more important for these medium-mass nuclei, not only for the actual ground-state energies, but also for the chiral truncation uncertainty estimates.

We interpret the differences in the estimated truncation errors, emerging from using the considered schemes, as an intrinsic uncertainty of our approach to error analysis. It would be interesting to see if it can be reduced by performing a more refined analysis using Bayesian methods, which would also

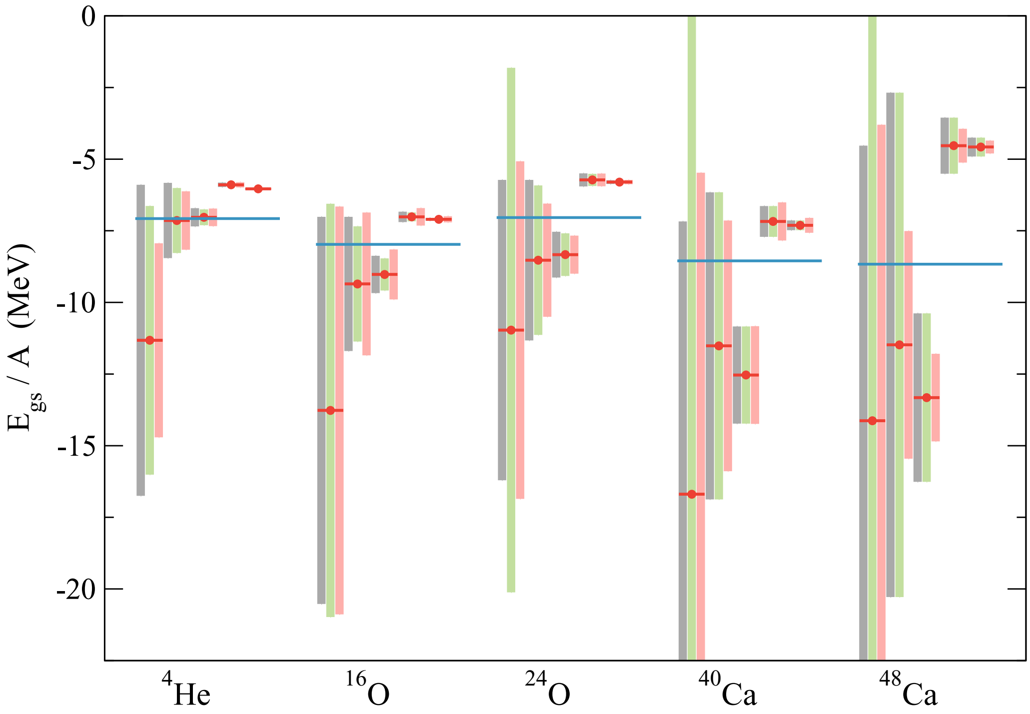

FIG. 17. Results for ground-state energies per nucleon of closed (sub)shell nuclei, showing chiral uncertainties as presented in the Introduction (gray bars) compared with the two alternative uncertainty estimates (green and pale red bars), discussed in the text. No numerical many-body uncertainties are shown. All results correspond to $R = 1.0$ fm and SRG $\alpha = 0.08$ fm^4 except for ^{48}Ca at N^{3}LO, where the results for $\alpha = 0.04$ fm^4 were taken due to the unavailability of the ones for $\alpha = 0.08$ fm^4. For comparison, the experimental values are also shown as the blue bars.

provide a statistical interpretation of the theoretical error bars [37,38].

VI. SUMMARY AND CONCLUSIONS

In this paper, we performed a comprehensive study of few- and many-nucleon observables based on the SCS chiral NN potentials of Refs. [13,14]. The pertinent results of our calculations can be summarized as follows:

(1) We have analyzed various nd elastic scattering and breakup observables and estimated truncation errors at different orders of the chiral expansion. Similarly to other calculations, we observe a considerable underprediction of the nd elastic scattering analyzing power A_y at low energy starting from N^{2}LO, the feature commonly referred to as the A_y-puzzle. At intermediate energies, the discrepancies between the calculated elastic scattering observables based on NN forces only and experimental data are, in many cases, significantly larger than the theoretical uncertainty at N^{3}LO and N^{4}LO and agree well with the expected size of the 3NF contributions. This makes elastic nucleon-deuteron scattering in this energy range a particularly promising testing ground for the chiral 3NF. However, the considered breakup observables are well reproduced, leaving little room for possible 3NF effects except for the symmetric space star configuration at low energy, where large deviations are observed. For these observables, known to represent another low-energy puzzle, our calculations agree with the ones based on other phenomenological and chiral EFT nuclear forces, and the truncation errors turn out to be very small.

(2) We have calculated various properties of $A = 3, 4$ nuclei in the framework of the Faddeev-Yakubovsky equations and studied light p-shell nuclei using the NCCI method. In the latter case, we were able to perform calculations at all chiral orders without SRG transformations for $A \leqslant 6$ using the cutoffs $R = 0.9$, 1.0, and 1.1 fm. For heavier nuclei, we had to rely on SRG evolution starting from N^{3}LO to achieve converged results. We found a qualitatively similar convergence pattern in all considered cases, namely a significant overbinding at LO, results close to the experimental values at NLO and N^{2}LO and underbinding at N^{3}LO and N^{4}LO. We have also calculated ground-state magnetic moments of light nuclei based on the single-nucleon current operator and estimated the corresponding NCCI extrapolation and truncation errors.

(3) To obtain results for medium-mass nuclei, we have performed state-of-the-art calculations within the coupled-cluster and in-medium similarity renormalization group frameworks. The obtained results for the ground-state energies of ^{16,24}O and ^{40,48}Ca show a similar pattern to that for light nuclei with the amount of overbinding (underbinding) at LO, NLO, and N^{2}LO (N^{3}LO and N^{4}LO) tending to increase with the number of nucleons A. The slower convergence of the chiral expansion for heavier nuclei is to be expected and reflects the increasing sensitivity to higher-momentum components of the interaction. The calculated charge radii of the considered medium-mass nuclei show a systematic improvement with the chiral order, but remain underestimated at N^{4}LO.

(4) Finally, we have addressed the reliability of our error analysis by exploring alternative approaches for uncertainty quantifications. We found, in general, a satisfactory agreement between all considered methods.

Our results demonstrate that the SCS chiral NN potentials are well suited for *ab initio* few- and many-body calculations and provide a natural reference point for systematic studies of 3NF effects and specific details of the NN interactions such as the choice of the basis of contact interactions and regularization schemes. It would be interesting to perform similar calculations using the new SMS chiral NN potentials of Ref. [25], which provide an outstanding description of neutron-proton and proton-proton scattering data below $E_{\text{lab}} = 300$ MeV and are considerably softer than the SCS potentials starting from N^{3}LO. Such a study would, in particular, bring insights into the role of the redundant contact interactions at N^{3}LO. Notice that the new SMS interactions also provide the flexibility to propagate statistical uncertainties of the NN LECs and to quantify the error from the uncertainty in the πN LECs and the choice of the energy range used in the determination of the NN contact interactions. Finally, and most importantly, the calculations should be extended by the inclusion of the consistent 3NFs [27,59,139–143]. Work along these lines is in progress by the LENPIC Collaboration [144].

ACKNOWLEDGMENTS

This work was supported by BMBF (Contracts No. 05P2015-NUSTAR R&D and No. 05P15RDFN1-NUSTAR.DA), the ERC Projects No. 259218 NUCLEAREFT and No. 307986 STRONGINT, by the DFG (SFB 1245), by DFG (TRR 110) and NSFC (1621131001), by the Polish National Science Center under Grants No. 2016/22/M/ST2/00173 and No. 2016/21/D/ST2/01120, by VolkswagenStiftung (Grant No. 93562) and by the Chinese Academy of Sciences (CAS) President's International Fellowship Initiative (PIFI) (Grant No. 2018DM0034). In addition, this research was supported in part by the National Science Foundation under Grants No. NSF PHY11-25915 and No. NSF PHY16-14460, by the U.S. Department of Energy under Grants No. DE-FG02-87ER40371, No. DESC0008485, No. DE-SC0008533, No. DESC0018223, and No. DESC0015376. This research used resources of the National Energy Research Scientific Computing Center (NERSC) and the Argonne Leadership Computing Facility (ALCF), which are U.S. Department of Energy Office of Science user facilities, supported under Contracts No. DE-AC02-05CH11231 and No. DE-AC02-06CH11357, and computing resources

TABLE X. Hartree-Fock results (rows without asterisk) and NCCI results (rows with asterisk) for the average relative momentum (in MeV/c) between a pair of nucleons in ^{3}H, ^{3,4,6,8}He and ^{6,8,9}Li as defined in Eq. (26). The first five columns of results correspond to the chiral orders from LO to N^{4}LO,xht while the last column is the average over the five columns of results. The rows are labeled by the value of the regularization parameter R. Hartree-Fock results are from the expectation value of the SRG-transformed kinetic energy operator with the SRG parameter $\alpha = 0.08\,\mathrm{fm}^4$. The first two rows for each nucleus are obtained with spherical Hartree-Fock using the filling fraction approximation appropriate to the specified nucleus. Rows with results from an NCCI calculation (labeled with an asterisk) use the bare NN interaction and the bare relative kinetic energy operator, extrapolated to the infinite matrix limit. We quote the Yakubovsky results for ^{4}He at N^{3}LO and N^{4}LO for their higher precision.

R [fm]	$p_{\mathrm{avg}}^{(0)}$	$p_{\mathrm{avg}}^{(2)}$	$p_{\mathrm{avg}}^{(3)}$	$p_{\mathrm{avg}}^{(4)}$	$p_{\mathrm{avg}}^{(5)}$	p_{avg}
^{3}H						
0.9	158.3	125.2	123.0	116.7	116.8	128.0
1.0	149.8	123.8	121.5	111.6	112.9	123.9
1.0*	144.0	126.0	124.0			
^{3}He						
0.9	157.3	123.9	121.6	115.4	115.6	126.8
1.0	148.7	122.5	120.1	110.4	111.7	122.7
^{4}He						
0.9	192.9	147.9	145.8	132.8	133.1	150.5
1.0	180.6	146.3	144.0	126.7	128.4	145.2
1.0*	180.0	147.0	145.0	176.8	169.6	163.6
^{6}He						
0.9	163.8	141.4	135.1	124.0	123.7	137.6
1.0	156.3	139.6	133.9	119.0	120.4	133.8
1.0*	157.0	137.0	132.0			
^{8}He						
0.9	153.3	146.8	136.0	124.0	123.1	136.6
1.0	148.1	144.4	135.1	118.9	120.1	133.3
1.0*	150.0	141.0	131.0			
^{6}Li						
0.9	166.6	143.5	137.1	125.6	125.3	139.6
1.0	159.4	141.8	135.9	120.4	121.9	135.9
1.0*	160.0	140.0	136.0			
^{8}Li						
0.9	165.9	151.7	141.9	128.3	127.3	143.0
1.0	159.5	149.5	140.9	122.9	124.3	139.4
1.0*	163.0	148.0	140.0			
^{9}Li						
0.9	166.5	155.8	144.4	129.8	128.4	145.0
1.0	160.2	153.5	143.4	124.1	125.4	141.3
1.0*	163.0	152.0	142.0			

TABLE XI. Same as table X but for ^{8,9}Be, ^{16,24}O, and ^{40,48}Ca.

R [fm]	$p_{\mathrm{avg}}^{(0)}$	$p_{\mathrm{avg}}^{(2)}$	$p_{\mathrm{avg}}^{(3)}$	$p_{\mathrm{avg}}^{(4)}$	$p_{\mathrm{avg}}^{(5)}$	p_{avg}
^{8}Be						
0.9	174.8	150.3	142.2	128.7	127.8	144.8
1.0	166.7	148.7	141.2	123.2	124.6	140.9
1.0*	176.0	149.0	144.0			
^{9}Be						
0.9	175.5	156.7	146.7	131.5	130.2	148.1
1.0	167.8	154.7	145.7	125.6	127.0	144.2
1.0*	173.0	153.0	146.0			
^{16}O						
0.9	223.1	177.2	169.2	148.3	145.0	172.5
1.0	210.3	176.5	167.6	140.6	141.0	167.2
1.0*	209.0	173.0	164.0			
^{24}O						
0.9	211.7	186.1	179.8	153.6	147.9	175.8
1.0	201.3	185.4	178.7	145.2	144.4	171.0
^{40}Ca						
0.9	249.5	196.1	203.5	168.0	159.0	195.2
1.0	234.4	198.2	203.2	158.5	155.7	190.0
^{48}Ca						
0.9	244.8	203.8	222.4	178.1	167.1	203.2
1.0	230.9	206.2	221.9	174.2	169.8	200.6

provided under the INCITE award "Nuclear Structure and Nuclear Reactions" from the U.S. Department of Energy, Office of Advanced Scientific Computing Research. Further computing resources were provided by the TU Darmstadt (lichtenberg) and on JUQUEEN and JURECA of the Jülich Supercomputing Centre, Jülich, Germany.

APPENDIX: EXPECTATION VALUES OF THE KINETIC ENERGY IN LIGHT- AND MEDIUM-MASS NUCLEI

In this appendix we provide some details on the estimation of the expansion parameter used to quantify the theoretical uncertainties for the ground-state properties of light- and medium-mass nuclei. As explained in Sec. III, this is achieved by inferring the relevant momentum scale from the expectation values of the SRG-transformed kinetic energy operator T. In Tables X and XI, we list our Hartree-Fock results for all nuclei considered in this paper for the cutoff values of $R = 0.9\,\mathrm{fm}$ and $R = 1.0\,\mathrm{fm}$. The resulting values of the momentum scale given in the last column of this table are obtained by taking the average over all chiral orders i of the quantity $\sqrt{2m_N\langle T\rangle^{(i)}/A}$.

[1] E. Epelbaum, H. W. Hammer, and U.-G. Meißner, Rev. Mod. Phys. **81**, 1773 (2009).

[2] R. Machleidt and D. R. Entem, Phys. Rep. **503**, 1 (2011).

[3] S. Weinberg, Phys. Lett. B **251**, 288 (1990).

[4] S. Weinberg, Nucl. Phys. B **363**, 3 (1991).

[5] A. Nogga, R. G. E. Timmermans, and U. van Kolck, Phys. Rev. C **72**, 054006 (2005).

[6] M. C. Birse, Phys. Rev. C **74**, 014003 (2006).

[7] M. Pavon Valderrama, Phys. Rev. C **83**, 024003 (2011).

[8] E. Epelbaum and J. Gegelia, Phys. Lett. B **716**, 338 (2012).

[9] A. M. Gasparyan, M. F. M. Lutz, and E. Epelbaum, Eur. Phys. J. A **49**, 115 (2013).

[10] J. A. Oller, Phys. Rev. C **93**, 024002 (2016).

[11] D. R. Entem, N. Kaiser, R. Machleidt, and Y. Nosyk, Phys. Rev. C **91**, 014002 (2015).

[12] D. R. Entem, N. Kaiser, R. Machleidt, and Y. Nosyk, Phys. Rev. C **92**, 064001 (2015).

[13] E. Epelbaum, H. Krebs, and U.-G. Meißner, Eur. Phys. J. A **51**, 53 (2015).

[14] E. Epelbaum, H. Krebs, and U.-G. Meißner, Phys. Rev. Lett. **115**, 122301 (2015).

[15] D. R. Entem, R. Machleidt, and Y. Nosyk, Phys. Rev. C **96**, 024004 (2017).

[16] M. Piarulli, L. Girlanda, R. Schiavilla, R. N. Perez, J. E. Amaro and E. R. Arriola, Phys. Rev. C **91**, 024003 (2015).

[17] B. D. Carlsson, A. Ekstrom, C. Forssen, D. F. Stromberg, G. R. Jansen, O. Lilja, M. Lindby, B. A. Mattsson, and K. A. Wendt, Phys. Rev. X **6**, 011019 (2016).

[18] M. Piarulli, L. Girlanda, R. Schiavilla, A. Kievsky, A. Lovato, L. E. Marcucci, S. C. Pieper, M. Viviani, and R. B. Wiringa, Phys. Rev. C **94**, 054007 (2016).

[19] A. Ekström, G. Hagen, T. D. Morris, T. Papenbrock, and P. D. Schwartz, Phys. Rev. C **97**, 024332 (2018).

[20] D. R. Entem and R. Machleidt, Phys. Rev. C **68**, 041001 (2003).

[21] E. Epelbaum, W. Glöckle, and Ulf-G. Meißner, Nucl. Phys. A **747**, 362 (2005).

[22] A. Gezerlis, I. Tews, E. Epelbaum, S. Gandolfi, K. Hebeler, A. Nogga, and A. Schwenk, Phys. Rev. Lett. **111**, 032501 (2013).

[23] A. Gezerlis, I. Tews, E. Epelbaum, M. Freunek, S. Gandolfi, K. Hebeler, A. Nogga, and A. Schwenk, Phys. Rev. C **90**, 054323 (2014).

[24] A. Dyhdalo, R. J. Furnstahl, K. Hebeler, and I. Tews, Phys. Rev. C **94**, 034001 (2016).

[25] P. Reinert, H. Krebs, and E. Epelbaum, Eur. Phys. J. A **54**, 86 (2018).

[26] M. Hoferichter, J. Ruiz de Elvira, B. Kubis, and Ulf-G. Meißner, Phys. Rev. Lett. **115**, 192301 (2015).

[27] H. Krebs, A. Gasparyan, and E. Epelbaum, Phys. Rev. C **85**, 054006 (2012).

[28] J. M. Alarcon, J. Martin Camalich and J. A. Oller, Ann. Phys. **336**, 413 (2013).

[29] Y. H. Chen, D. L. Yao, and H. Q. Zheng, Phys. Rev. D **87**, 054019 (2013).

[30] K. A. Wendt, B. D. Carlsson, and A. Ekström, arXiv:1410.0646.

[31] D. L. Yao, D. Siemens, V. Bernard, E. Epelbaum, A. M. Gasparyan, J. Gegelia, H. Krebs, and U.-G. Meißner, J. High Energy Phys. 05 (2016) 038.

[32] D. Siemens, V. Bernard, E. Epelbaum, A. Gasparyan, H. Krebs, and Ulf-G. Meißner, Phys. Rev. C **94**, 014620 (2016).

[33] D. Siemens, J. Ruiz de Elvira, E. Epelbaum, M. Hoferichter, H. Krebs, B. Kubis, and U.-G. Meißner, Phys. Lett. B **770**, 27 (2017).

[34] D. Siemens, V. Bernard, E. Epelbaum, A. M. Gasparyan, H. Krebs, and Ulf-G. Meißner, Phys. Rev. C **96**, 055205 (2017).

[35] M. Hoferichter, J. Ruiz de Elvira, B. Kubis, and U.-G. Meißner, Phys. Rep. **625**, 1 (2016).

[36] V. G. J. Stoks, R. A. M. Klomp, C. P. F. Terheggen, and J. J. de Swart, Phys. Rev. C **49**, 2950 (1994).

[37] R. J. Furnstahl, N. Klco, D. R. Phillips, and S. Wesolowski, Phys. Rev. C **92**, 024005 (2015).

[38] J. A. Melendez, S. Wesolowski, and R. J. Furnstahl, Phys. Rev. C **96**, 024003 (2017).

[39] J. E. Lynn, I. Tews, J. Carlson, S. Gandolfi, A. Gezerlis, K. E. Schmidt, and A. Schwenk, Phys. Rev. Lett. **116**, 062501 (2016).

[40] J. E. Lynn, I. Tews, J. Carlson, S. Gandolfi, A. Gezerlis, K. E. Schmidt, and A. Schwenk, Phys. Rev. C **96**, 054007 (2017).

[41] D. Lonardoni, J. Carlson, S. Gandolfi, J. E. Lynn, K. E. Schmidt, A. Schwenk, and X. B. Wang, Phys. Rev. Lett. **120**, 122502 (2018).

[42] D. Lonardoni, S. Gandolfi, J. E. Lynn, C. Petrie, J. Carlson, K. E. Schmidt, and A. Schwenk, Phys. Rev. C **97**, 044318 (2018).

[43] S. Binder, A. Calci, E. Epelbaum, R. J. Furnstahl, J. Golak, K. Hebeler, H. Kamada, H. Krebs, J. Langhammer, S. Liebig, P. Maris, Ulf-G. Meißner, D. Minossi, A. Nogga, H. Potter, R. Roth, R. Skibinski, K. Topolnicki, J. P. Vary, and H. Witała, (LENPIC Collaboration), Phys. Rev. C **93**, 044002 (2016).

[44] R. Skibiński, J. Golak, K. Topolnicki, H. Witala, E. Epelbaum, H. Krebs, H. Kamada, Ulf-G. Meißner, and A. Nogga, Phys. Rev. C **93**, 064002 (2016).

[45] J. Hu, Y. Zhang, E. Epelbaum, Ulf-G. Meißner, and J. Meng, Phys. Rev. C **96**, 034307 (2017).

[46] O. J. Hernandez, A. Ekström, N. Nevo Dinur, C. Ji, S. Bacca, and N. Barnea, Phys. Lett. B **778**, 377 (2018).

[47] H. Witała, T. Cornelius, and W. Glöckle, Few-Body Syst. **3**, 123 (1988).

[48] W. Glöckle, H. Witała, D. Hüber, H. Kamada, and J. Golak, Phys. Rep. **274**, 107 (1996).

[49] D. Hüber, H. Kamada, H. Witała, and W. Glöckle, Acta Phys. Pol. **B28**, 1677 (1997).

[50] W. Glöckle, *The Quantum Mechanical Few-Body Problem* (Springer-Verlag, Berlin, 1983).

[51] R. B. Wiringa, V. G. J. Stoks, and R. Schiavilla, Phys. Rev. C **51**, 38 (1995).

[52] R. Machleidt, F. Sammarruca, and Y. Song, Phys. Rev. C **53**, R1483 (1996).

[53] S. A. Coon and H. K. Han, Few-Body Syst. **30**, 131 (2001).

[54] B. S. Pudliner, V. R. Pandharipande, J. Carlson, S. C. Pieper, and R. B. Wiringa, Phys. Rev. C **56**, 1720 (1997).

[55] W. Tornow *et al.*, Phys. Lett. B **257**, 273 (1991).

[56] W. Tornow, C. R. Howell, R. C. Byrd, R. S. Pedroni, and R. L. Walter, Phys. Rev. Lett. **49**, 312 (1982).

[57] W. Tornow, R. C. Byrd, C. R. Howell, R. S. Pedroni, and R. L. Walter, Phys. Rev. C **27**, 2439 (1983).

[58] E. Epelbaum, Prog. Part. Nucl. Phys. **57**, 654 (2006).

[59] E. Epelbaum, A. Nogga, W. Glockle, H. Kamada, Ulf-G. Meißner, and H. Witala, Phys. Rev. C **66**, 064001 (2002).

[60] J. R. Bergervoet, P. C. van Campen, R. A. M. Klomp, J. L. de Kok, T. A. Rijken, V. G. J. Stoks, and J. J. de Swart, Phys. Rev. C **41**, 1435 (1990).

[61] V. G. J. Stoks, R. A. M. Klomp, M. C. M. Rentmeester, and J. J. de Swart, Phys. Rev. C **48**, 792 (1993).

[62] L. Girlanda, A. Kievsky, and M. Viviani, Phys. Rev. C **84**, 014001 (2011).

[63] N. Sakamoto *et al.*, Phys. Lett. B **367**, 60 (1996).

[64] H. Sakai, K. Sekiguchi, H. Witała, W. Glöckle, M. Hatano, H. Kamada, H. Kato, Y. Maeda, A. Nogga, T. Ohnishi, H. Okamura, N. Sakamoto, S. Sakoda, Y. Satou, K. Suda, A. Tamii,

T. Uesaka, T. Wakasa, and K. Yako, Phys. Rev. Lett. **84**, 5288 (2000).

[65] K. Sekiguchi, H. Sakai, H. Witała, W. Glöckle, J. Golak, M. Hatano, H. Kamada, H. Kato, Y. Maeda, J. Nishikawa, A. Nogga, T. Ohnishi, H. Okamura, N. Sakamoto, S. Sakoda, Y. Satou, K. Suda, A. Tamii, T. Uesaka, T. Wakasa, and K. Yako, Phys. Rev. C **65**, 034003 (2002).

[66] K. Sekiguchi, H. Sakai, H. Witała, K. Ermisch, W. Glockle, J. Golak, M. Hatano, H. Kamada, N. Kalantar-Nayestanaki, H. Kato, Y. Maeda, J. Nishikawa, A. Nogga, T. Ohnishi, H. Okamura, T. Saito, N. Sakamoto, S. Sakoda, Y. Satou, K. Suda, A. Tamii, T. Uchigashima, T. Uesaka, T. Wakasa, and K. Yako, Phys. Rev. C **70**, 014001 (2004).

[67] N. Kalantar-Nayestanaki, E. Epelbaum, J. G. Messchendorp, and A. Nogga, Rep. Prog. Phys. **75**, 016301 (2012).

[68] H. Witała and W. Glöckle, J. Phys. G: Nucl. Part. Phys. **37**, 064003 (2010).

[69] A. Siepe, J. Deng, V. Huhn, L. Wätzold, C. Weber, W. von Witsch, H. Witała, and W. Glöckle, Phys. Rev. C **65**, 034010 (2002).

[70] X. C. Ruan, Z. Y. Zhou, X. Li, J. Jiang, H. X. Huang, Q. P. Zhong, H. Q. Tang, B. J. Qi, J. Bao, B. Xin, W. von Witsch, and H. Witała, Phys. Rev. C **75**, 057001 (2007).

[71] H. Witała and W. Glöckle, Phys. Rev. C **83**, 034004 (2011).

[72] H. Witała and W. Glöckle, Phys. Rev. C **85**, 064003 (2012).

[73] H. R. Setze *et al.*, Phys. Lett. B **388**, 229 (1996).

[74] J. Strate *et al.*, J. Phys. G: Nucl. Phys. **14**, L229 (1988).

[75] J. Strate *et al.*, Nucl. Phys. A **501**, 51 (1989).

[76] G. Rauprich *et al.*, Nucl. Phys. A **535**, 313 (1991).

[77] J. Zejma, M. Allet, K. Bodek, J. Lang, R. Müller, S. Navert, O. Naviliat-Cuncic, J. Sromicki, E. Stephan, L. Jarczyk, S. Kistryn, J. Smyrski, A. Strzałkowski, W. Glöckle, J. Golak, D. Huber, H. Witała, and P. A. Schmelzbach, Phys. Rev. C **55**, 42 (1997).

[78] M. Allet *et al.*, Few-Body Syst. **20**, 27 (1996).

[79] K. Sagara, Few-Body Syst. **48**, 59 (2010).

[80] A. Deltuva, A. C. Fonseca, and P. U. Sauer, Phys. Rev. C **72**, 054004 (2005).

[81] F. Takeutchi, T. Yuasa, K. Kuroda, and Y. Sakamoto, Nucl. Phys. A **152**, 434 (1970).

[82] A. Nogga, H. Kamada, W. Glöckle, and B. R. Barrett, Phys. Rev. C **65**, 054003 (2002).

[83] J. Hoppe, C. Drischler, R. J. Furnstahl, K. Hebeler, and A. Schwenk, Phys. Rev. C **96**, 054002 (2017).

[84] B. R. Barrett, P. Navratil, and J. P. Vary, Prog. Part. Nucl. Phys. **69**, 131 (2013).

[85] P. Maris, J. P. Vary, and A. M. Shirokov, Phys. Rev. C **79**, 014308 (2009).

[86] P. Maris and J. P. Vary, Int. J. Mod. Phys. E **22**, 1330016 (2013).

[87] S. A. Coon, M. I. Avetian, M. K. G. Kruse, U. van Kolck, P. Maris, and J. P. Vary, Phys. Rev. C **86**, 054002 (2012).

[88] R. J. Furnstahl, G. Hagen, and T. Papenbrock, Phys. Rev. C **86**, 031301 (2012).

[89] S. N. More, A. Ekström, R. J. Furnstahl, G. Hagen, and T. Papenbrock, Phys. Rev. C **87**, 044326 (2013).

[90] K. A. Wendt, C. Forssén, T. Papenbrock, and D. Sääf, Phys. Rev. C **91**, 061301 (2015).

[91] S. D. Glazek and K. G. Wilson, Phys. Rev. D **48**, 5863 (1993).

[92] F. Wegner, Ann. der Phys. **506**, 77 (1994).

[93] S. K. Bogner, R. J. Furnstahl, P. Maris, R. J. Perry, A. Schwenk, and J. P. Vary, Nucl. Phys. A **801**, 21 (2008).

[94] S. K. Bogner, R. J. Furnstahl, and A. Schwenk, Prog. Part. Nucl. Phys. **65**, 94 (2010).

[95] E. D. Jurgenson, P. Navratil, and R. J. Furnstahl, Phys. Rev. Lett. **103**, 082501 (2009).

[96] R. Roth, J. Langhammer, A. Calci, S. Binder, and P. Navratil, Phys. Rev. Lett. **107**, 072501 (2011).

[97] E. D. Jurgenson, P. Maris, R. J. Furnstahl, P. Navratil, W. E. Ormand, and J. P. Vary, Phys. Rev. C **87**, 054312 (2013).

[98] R. Roth, A. Calci, J. Langhammer, and S. Binder, Phys. Rev. C **90**, 024325 (2014).

[99] P. Maris, M. Sosonkina, J. P. Vary, E. Ng, and C. Yang, Proc. Comp. Sci. **1**, 97 (2010).

[100] H. M. Aktulga, C. Yang, E. G. Ng, P. Maris, and J. P. Vary, Concurrency Computat.: Pract. Exper. **26**, 2631 (2014).

[101] J. P. Vary, P. Maris, E. Ng, C. Yang, and M. Sosonkina, J. Phys. Conf. Ser. **180**, 012083 (2009).

[102] P. Navratil, V. G. Gueorguiev, J. P. Vary, W. E. Ormand, and A. Nogga, Phys. Rev. Lett. **99**, 042501 (2007).

[103] S. Kölling, E. Epelbaum, H. Krebs, and U.-G. Meißner, Phys. Rev. C **80**, 045502 (2009).

[104] S. Kölling, E. Epelbaum, H. Krebs, and U.-G. Meißner, Phys. Rev. C **84**, 054008 (2011).

[105] H. Krebs, E. Epelbaum, and U.-G. Meißner, Annals Phys. **378**, 317 (2017).

[106] S. Pastore, R. Schiavilla, and J. L. Goity, Phys. Rev. C **78**, 064002 (2008).

[107] S. Pastore, S. C. Pieper, R. Schiavilla, and R. B. Wiringa, Phys. Rev. C **87**, 035503 (2013).

[108] A. Baroni, L. Girlanda, S. Pastore, R. Schiavilla, and M. Viviani, Phys. Rev. C **93**, 015501 (2016); **93**, 049902(E) (2016); **95**, 059901(E) (2017).

[109] G. Hagen, T. Papenbrock, D. J. Dean, A. Schwenk, A. Nogga, M. Wloch, and P. Piecuch, Phys. Rev. C **76**, 034302 (2007).

[110] G. Hagen, T. Papenbrock, D. J. Dean, and M. Hjorth-Jensen, Phys. Rev. C **82**, 034330 (2010).

[111] S. Binder, J. Langhammer, A. Calci, P. Navratil, and R. Roth, Phys. Rev. C **87**, 021303 (2013).

[112] G. R. Jansen, Phys. Rev. C **88**, 024305 (2013).

[113] S. Binder, P. Piecuch, A. Calci, J. Langhammer, P. Navratil, and R. Roth, Phys. Rev. C **88**, 054319 (2013).

[114] G. Hagen and N. Michel, Phys. Rev. C **86**, 021602 (2012).

[115] G. Baardsen, A. Ekström, G. Hagen, and M. Hjorth-Jensen, Phys. Rev. C **88**, 054312 (2013).

[116] G. Hagen, M. Hjorth-Jensen, G. R. Jansen, R. Machleidt, and T. Papenbrock, Phys. Rev. Lett. **109**, 032502 (2012).

[117] G. Hagen, M. Hjorth-Jensen, G. R. Jansen, R. Machleidt, and T. Papenbrock, Phys. Rev. Lett. **108**, 242501 (2012).

[118] G. Hagen, T. Papenbrock, M. Hjorth-Jensen, and D. J. Dean, Rept. Prog. Phys. **77**, 096302 (2014).

[119] I. Shavitt and R. J. Bartlett, *Many-Body Methods in Chemistry and Physics* (Cambridge University Press, Cambridge, 2009).

[120] K. Raghavachari, G. W. Trucks, J. A. Pople, and M. Head-Gordon, Chem. Phys. Lett. **157**, 479 (1989).

[121] A. G. Taube and R. J. Bartlett, J. Chem. Phys. **128**, 044110 (2008).

[122] A. G. Taube and R. J. Bartlett, J. Chem. Phys. **128**, 044111 (2008).

[123] P. Piecuch, J. R. Gour, and M. Włoch, Int. J. Quantum Chem. **109**, 3268 (2009).

[124] R. Roth, S. Binder, K. Vobig, A. Calci, J. Langhammer, and P. Navratil, Phys. Rev. Lett. **109**, 052501 (2012).

[125] K. Tsukiyama, S. K. Bogner, and A. Schwenk, Phys. Rev. Lett. **106**, 222502 (2011).

[126] H. Hergert, S. K. Bogner, S. Binder, A. Calci, J. Langhammer, R. Roth, and A. Schwenk, Phys. Rev. C **87**, 034307 (2013).

[127] H. Hergert, S. K. Bogner, T. D. Morris, A. Schwenk, and K. Tsukiyama, Phys. Rep. **621**, 165 (2016).

[128] H. Hergert, Phys. Scr. **92**, 023002 (2017).

[129] K. Tsukiyama, S. K. Bogner, and A. Schwenk, Phys. Rev. C **85**, 061304 (2012).

[130] S. K. Bogner, H. Hergert, J. D. Holt, A. Schwenk, S. Binder, A. Calci, J. Langhammer, and R. Roth, Phys. Rev. Lett. **113**, 142501 (2014).

[131] S. R. Stroberg, A. Calci, H. Hergert, J. D. Holt, S. K. Bogner, R. Roth, and A. Schwenk, Phys. Rev. Lett. **118**, 032502 (2017).

[132] H. Hergert, S. Binder, A. Calci, J. Langhammer, and R. Roth, Phys. Rev. Lett. **110**, 242501 (2013).

[133] H. Hergert, S. K. Bogner, T. D. Morris, S. Binder, A. Calci, J. Langhammer, and R. Roth, Phys. Rev. C **90**, 041302 (2014).

[134] E. Gebrerufael, K. Vobig, H. Hergert, and R. Roth, Phys. Rev. Lett. **118**, 152503 (2017).

[135] A. Ekström, G. R. Jansen, K. A. Wendt, G. Hagen, T. Papenbrock, B. D. Carlsson, C. Forssén, M. Hjorth-Jensen, P. Navrátil, and W. Nazarewicz, Phys. Rev. C **91**, 051301(R) (2015).

[136] P. Navratil, Few Body Syst. **41**, 117 (2007).

[137] E. Epelbaum, J. Gegelia, and U.-G. Meißner, Nucl. Phys. B **925**, 161 (2017).

[138] B. von Przewoski *et al.*, Phys. Rev. C **74**, 064003 (2006).

[139] U. van Kolck, Phys. Rev. C **49**, 2932 (1994).

[140] V. Bernard, E. Epelbaum, H. Krebs, and Ulf-G. Meißner, Phys. Rev. C **77**, 064004 (2008).

[141] V. Bernard, E. Epelbaum, H. Krebs, and Ulf-G. Meißner, Phys. Rev. C **84**, 054001 (2011).

[142] H. Krebs, A. Gasparyan, and E. Epelbaum, Phys. Rev. C **87**, 054007 (2013).

[143] E. Epelbaum, A. M. Gasparyan, H. Krebs, and C. Schat, Eur. Phys. J. A **51**, 26 (2015).

[144] K. Hebeler, H. Krebs, E. Epelbaum, J. Golak, and R. Skibiński, Phys. Rev. C **91**, 044001 (2015).